TECHNICAL REPORT

Demonstration Of Advanced EMI Models For Live-Site UXO Discrimination At Former Camp Butner, North Carolina

SERDP Project MR-1572

MAY 2012

Fridon Shubitidze
Sky Research, Inc.

This document has been cleared for public release

SERDP
DOD ▪ EPA ▪ DOE

This report was prepared under contract to the Department of Defense Strategic Environmental Research and Development Program (SERDP). The publication of this report does not indicate endorsement by the Department of Defense, nor should the contents be construed as reflecting the official policy or position of the Department of Defense. Reference herein to any specific commercial product, process, or service by trade name, trademark, manufacturer, or otherwise, does not necessarily constitute or imply its endorsement, recommendation, or favoring by the Department of Defense.

Table of Contents

1 INTRODUCTION 1
1.1 Background 1
1.2 Brief site history 2
1.3 Objective of the demonstration 2
2 TECHNOLOGY 3
2.1 The orthonormalized volume magnetic source model 3
2.2 Joint diagonalization data preprocessing 4
2.3 EMI Data inversion: A global optimization technique 5
2.3.1 Discrimination parameters 6
2.3.2 Classification approaches 6
2.3.3 Classification using template matching 7
2.4 Details of classification schemes 7
2.4.1 Camp Butner TEMTADS data inversion and classification scheme 9
2.4.2 Camp Butner MM data inversion and classification scheme 13
3 PERFORMANCE OBJECTIVES 18
3.1 Objective: maximize correct classification of munitions 19
3.1.1 Metric 19
3.1.2 Data requirements 19
3.1.3 Success criteria evaluation and results 19
3.1.4 Results 19
3.2 Objective: maximize correct classification of non-munitions 19
3.2.1 Metric 19
3.2.2 Data requirements 20
3.2.3 Success criteria evaluation and results 20
3.2.4 Results 20
3.3 Objective: specify a no-dig threshold 20
3.3.1 Metric 20
3.3.2 Data requirements 20
3.3.3 Success criteria evaluation and results 20
3.3.4 Results 20
3.4 Objective: minimize the number of anomalies that cannot be analyzed 21

3.4.1 Metric ... 21
3.4.2 Data requirements ... 21
3.4.3 Success criteria evaluation and results ... 21
3.4.4 Results ... 21
3.5 Objective: correct estimation of target parameters ... 21
3.5.1 Metric ... 21
3.5.2 Data requirements ... 21
3.5.3 Success criteria evaluation and results ... 21
3.5.4 Results ... 22
4 TEST DESIGN ... 24
4.1 Site preparation ... 24
4.2 Demonstration schedule ... 24
5 DATA ANALYSIS PLAN ... 25
5.1 Extracting target locations ... 25
5.2 Extracting target intrinsic parameters ... 25
5.2.1 Single targets ... 25
5.2.2 Multi-target cases ... 25
5.3 Selection of intrinsic parameters for classification ... 26
5.4 Training ... 26
5.5 Classification ... 26
5.6 Decision memo ... 27
6 COST ASSESSMENT ... 28
7 MANAGEMENT AND STAFFING ... 29
8 REFERENCES ... 30
9 APPENDICES ... 33
9.1 Appendix A: Health and Safety Plan (HASP) ... 33
9.2 Appendix B: Points of Contact ... 33
9.3 Appendix C: ... 34
9.3.1 The orthonormalized volume magnetic source model ... 34
9.3.2 Orthonormal Green functions ... 36
9.3.3 ONVMS procedure ... 38
9.3.4 Joint diagonalization for multi-target data pre-processing ... 39
9.3.5 The multi-static response matrix ... 39

9.3.6 Interpretation and diagonalization of the MSR matrix 40
9.3.7 Algorithm for joint diagonalization 42

List of Figures

Figure 1. TEMTADS multi-static response matrix eigenvalues versus time for (top row) a 105-mm HE projectile and a 105-mm HEAT round, (center row) an M-48 Fuze and a 37-mm munition, and (third row) two clutter scenarios, one with two items (left) and another with several (right). 8

Figure 2. TEMTADS multi-static response matrix eigenvalues versus time for some samples of requested anomalies. 9

Figure 3: Inverted total ONVMS time-decay profiles for four Camp Butner targets: (top row) 105-mm HE munition and 105-mm HEAT round, and (bottom) M-48 Fuze and 37-mm projectile with copper band. 10

Figure 4: Inverted total ONVMS time-decay profiles for 37-mm projectiles without copper band. 11

Figure 5. ROC curve for the Camp Butner TEMTADS blind test. 12

Figure 6: *Left*: Scatter plot for all MM anomalies based on the extracted total ONVMS. *Right*: Probability function for all MM anomalies. 13

Figure 7: Inverted magnetic dipole polarizability (left) and total ONVMS (right) time-decay profiles for MM anomaly #2504. The thin red lines show a library sample, while the thick blue and green lines show the inversion results. 14

Figure 8. Inverted total ONVMS time-decay profiles from Camp Butner MM data sets: (top row) 105-mm HE shells and 105 mm HEAT rounds, (bottom row) M-48 Fuzes and 37-mm projectiles. 15

Figure 9. Inverted total ONVMS time-decay profiles from Camp Butner MM data sets for 37-mm projectiles without driving copper bands. 16

Figure 10: Result of the supervised clustering classification for the Camp Butner MM anomalies using the logarithms of $M_{zz}(t_1)$ / $M_{zz}(t_{30})$ and $M_{zz}(t_1)$. The supervised clustering was trained with calibration data. The green markers correspond to clutter and the red ones to TOI. 16

Figure 11: ROC curve for the Camp Butner MetalMapper blind test. 17

Figure 12. Estimated and actual depths for Camp Butner, NC MM anomalies. Actual depths were measured within a reasonable accuracy from the soil surface, and the estimated depths were calculated respect the MM z-Tx center. These facts explain a negligible deference's between the estimated and ground truth depths. 22

Figure 13. Estimated and actual depths for Camp Butner, NC TEMTADS anomalies. The estimated depth agrees to the ground truth result within acceptable tolerance. 23

Figure 14. Gantt chart showing a detailed schedule of the activities conducted at Camp Butner. 24

Figure 15: Project management hierarchy. 29

Figure 16: A metallic object under the transmitter. The target's EMI response at the receiver coil can be calculated from the equivalent surface or volume magnetic dipole moment ***d*m**. 36

List of Tables

Table 1: Performance objectives.....18
Table 2: Cost model for advanced EMI model demonstration at the former Camp Butner.....28
Table 3: Points of Contact for the advanced EMI models' demonstration.....33

List of Acronyms

AIC	Akaike Information Criterion
APG	Aberdeen Proving Ground
BIC	Bayesian Information Criterion
cm	Centimeter
DLL	Dynamic Link Libraries
DoD	Department of Defense
EM	Electromagnetic
EMA	Expectation Maximization Algorithm
EMI	Electromagnetic Induction
ESTCP	Environmental Security Technology Certification Program
FCS	Former Camp Sibert
GSEA	Generalized standardized excitation approach
IDA	Institute for Defense Analyses.
JD	Joint Diagonalization
MEG	Magneto encephalographic
ML	Maximum Likelihood
μs	Microsecond
mm	Millimeter
MM	MetalMapper
MPV	Man-Portable Vector
ms	Millisecond
MR	Munitions response
MSR	Multi-static response
MUSIC	Multiple Signal Classification
NC	North Carolina
NSMS	Normalized surface magnetic source
NV/SMS	Normalized volume or surface magnetic source models
ONVMS	Orthogonal normalized volume magnetic source
ONV/SMS	Orthonormalized volume or surface magnetic source models
PNN	Probabilistic Neural Network
SERDP	Strategic Environmental Research and Development Program
SLO	San Luis Obispo
SVM	Support vector machine
TD	Time Domain
TEMTADS	Time Domain Electromagnetic Towed Array Detection System
TOI	Target of Interest
UXO	Unexploded Ordnance

1 INTRODUCTION

This demonstration is designed to illustrate the discrimination performance at a challenging live-site of a suite of advanced electromagnetic induction (EMI) modeling approaches developed to go beyond the simple dipole model in accuracy and predictive ability. The core of the suite consists of the orthonormalized volume magnetic source (ONVMS) model for target characterization, a target-counting pre-processing procedure based on joint diagonalization (JD), and an implementation of the differential evolution (DE) algorithm for nonlinear optimization used to locate targets. The study used cued data sets collected at Camp Butner in North Carolina using two next-generation EMI sensors, the Geometrics MetalMapper (MM) and the Time-domain Electro-Magnetic Towed Array Detection System (TEMTADS) developed by the NRL and G&G Sciences. The site was contaminated with fuzes and a mix of 37-mm and 105-mm munitions. Each data set was inverted with the purpose of estimating the number of targets producing each anomaly and the parameters associated with each target, both extrinsic—its orientation, location and depth—and intrinsic—its total volume magnetic source amplitude (ONVMS), which depends on its size, shape and material properties. The inverted intrinsic parameters were then used to classify the targets, and in the end we generated sensor-specific dig-lists for each EMI instrument and submitted them to the Institute of Defense Analyses (IDA) for independent scoring.

1.1 Background

The Environmental Security Technology Certification Program (ESTCP) recently launched a series of live-site UXO blind tests taking place in increasingly challenging and complex sites [1-4]. The first classification study was conducted in 2007 at the UXO live-site at the former Camp Sibert in Alabama using two commercially available first-generation EMI sensors (the EM61-MK2 and the EM-63, both from Geonics) [1]. At that site, the discrimination test was relatively simple: one had to discriminate large intact 4.2″ mortars from smaller range scrap, shrapnel and cultural debris, and the anomalies were very well separated.

The second ESTCP discrimination study took place in 2009 at the live-UXO site at Camp San Luis Obispo (SLO) in California and featured a more challenging topography and a wider mix of targets of interest (TOI) [4]. Magnetometers and first-generation EMI sensors (again the Geonics EM61-MK2) were deployed on the site and used in survey mode for a first screening. Afterwards, two advanced EMI sensing systems—the Berkeley UXO Discriminator (BUD) and the Naval Research Laboratory's TEMTADS array—were used to perform cued interrogation of a number of the anomalies detected. A third advanced system, the Geometrics MetalMapper, was used in both survey and cued modes for anomaly identification and classification. Among the munitions buried at SLO were 60-mm, 81-mm, and 4.2″ mortars and 2.36″ rockets; three additional types of munitions were discovered during the course of the demonstration.

The third site was chosen to be the former Camp Butner in North Carolina [2]. This demonstration was designed to investigate evolving classification methodologies at a site densely contaminated with small UXO (in this case mostly 37-mm projectiles).

1.2 Brief site history

Please refer to the ESTCP Live Site Demonstration Plan [3].

1.3 Objective of the demonstration

The advanced EMI models we present here (ONVMS and JD) were developed under SERDP Project MM-1572 [5] and tested against TEMTADS data sets collected at the Aberdeen Proving Ground (APG) test site in Maryland and in a retrospective analysis of cued TEMTADS data collected at the San Luis Obispo site [6-10]. The present test of discrimination performance considers data taken at Camp Butner; this live site was densely contaminated with small targets such as 37-mm projectiles and fuzes, adding another level of complexity into the classification and thus further demonstrating the robustness of the advanced EMI models for live-site UXO discrimination.

Overall, the principal objective of this demonstration was to demonstrate the models' classification performance for live-site UXO problems. The specific technical objectives were to:

1. Demonstrate the advanced EMI models' classification accuracy and their applicability to live-site UXO discrimination problems.
2. Illustrate and document the robustness of the data inversion and discrimination models.
3. Invert targets' intrinsic parameters and identify robust classification features.
4. Indentify all seeded and native UXO.
5. Eliminate at least 75% of the targets that do not correspond to TOI.
6. Indentify sources of uncertainty in the classification process and include them in a dig/no-dig decision process.
7. Understand and document the applicability and limitations of the advanced EMI discrimination technologies in the context of project objectives, site characteristics, and suspected ordnance contamination.

2 TECHNOLOGY

The advanced EMI models and statistical signal processing approaches developed and tested over the past three years under SERDP Project MM-1572 [5] were able to detect and identify buried UXO ranging in caliber from 25 mm up to 155 mm. The technique was seen to be physically complete, fast, accurate, and clutter-tolerant, and provided excellent classification in both single- and multiple-target scenarios when combined with multi-axis/transmitter/receiver sensors like TEMTADS and MetalMapper [11]. We start our technology description with an overview in Section 2.1 of the orthonormalized volume magnetic source model, which we use to represent the signatures and extract the properties of multiple subsurface targets simultaneously in an efficient manner. We then discuss in Section 2.2 a data pre-processing approach based on joint diagonalization that often allows one to make certain judgments on the number and type of unknown targets without the need to perform inversion. In Section 2.3 we discuss our complete inversion procedure, which combines ONVMS with Differential Evolution optimization, and we conclude in Section 2.4 by presenting our classification procedures.

2.1 The orthonormalized volume magnetic source model

The advanced models we have developed for UXO discrimination include the normalized surface magnetic source (NSMS) model [12] and the orthonormalized volume magnetic source (ONVMS) model [13]. The ONVMS model can be considered as a generalized volume dipole model: in it, an object's response to a sensor is modeled mathematically using a set of equivalent point-like analytic solutions of the Maxwell equations (usually dipoles, though charges are also a possibility) distributed over a computational volume located under an EMI sensor and potentially containing anomalies. The amplitudes of the sources are proportional to the component of the primary magnetic field; once this dependence is normalized out, the ONVMS strengths are determined directly from the data using a set of orthogonal functions.

Overall, we make the usual EMI assumptions: we neglect displacement currents everywhere, as well as electric fields and conduction currents in air and soil. The primary magnetic field generated by the sensor penetrates the objects in its vicinity to some degree, inducing eddy currents and magnetic dipoles inside them, which, in turn, produce a secondary or scattered magnetic field. This is the field that we propose to represent as being due to a volumetric distribution of magnetic dipoles:

$$\mathbf{H}^{\mathrm{sc}}(\mathbf{r}, p) = \int_V \frac{1}{4\pi R^3}(3\hat{\mathbf{R}}\hat{\mathbf{R}} - \bar{\bar{\mathbf{I}}}) \cdot \mathbf{m}(\mathbf{r}_v', p)dv' = \int_V \bar{\bar{G}}(\mathbf{r}, \mathbf{r}_v') \cdot \mathbf{m}(\mathbf{r}_v', p)dv', \tag{1}$$

where $p = \{t, f\}$ is time or frequency, $\hat{\mathbf{R}}$ is the unit vector along $\mathbf{R} = \mathbf{r} - \mathbf{r}_v'$, $\mathbf{r}_v'$ is the position of the v'-th infinitesimal dipole in the volume V, $\mathbf{r}$ is the observation point, and $\bar{\bar{\mathbf{I}}}$ and $\bar{\bar{G}}(\mathbf{r}, \mathbf{r}_v')$ are respectively the identity and Green dyads. The induced magnetic dipole moment $\mathbf{m}(\mathbf{r}_v', p)$ at point $\mathbf{r}_v'$ on the surface is related to the primary field through $\mathbf{m}(\mathbf{r}_v', p) = \bar{\bar{\mathbf{M}}}(\mathbf{r}_v', p) \cdot \mathbf{H}^{\mathrm{pr}}(\mathbf{r}_v')$, where

$\bar{\bar{\mathbf{M}}}(\mathbf{r}'_v, p)$ is the symmetric polarizability tensor. The secondary magnetic field at any point can be expanded into a set of orthonormal functions $\bar{\bar{\psi}}_i(\mathbf{r})$ as

$$\mathbf{H}(\mathbf{r}) = \sum_{i=1}^{N_v} \bar{\bar{\psi}}_i(\mathbf{R}_i) \cdot \mathbf{b}_i \,, \tag{2}$$

where we have also introduced the expansion coefficients $\mathbf{b}_i$. The $\bar{\bar{\psi}}_i$ are linear combinations of dipole Green dyads and are guaranteed to be orthonormal as a result of the Gram-Schmidt orthogonalization procedure; thanks to this property, the amplitudes of the tensor elements $\bar{\bar{\mathbf{M}}}_i(p)$ can be determined without having to solve a linear system of equations. Two great advantages of ONVMS are that it takes into account the mutual couplings between different sections of the targets and that it avoids matrix singularity problems in multi-object cases. It treats single- and multi-target scenarios on the same footing. Once the tensor elements and locations of the responding dipoles are determined, one can group them in space and determine the total polarizability tensor within each group, which is then jointly-diagonalized in time to extract the temporal decay law of its diagonal elements. These diagonal elements have been shown to be intrinsic to the objects, and can be used, either on their own or in combination with other quantities, in discrimination processing [14]. The theoretical basis of the ONVMS model is outlined in Appendix C.

2.2 Joint diagonalization data preprocessing

Advanced electromagnetic induction (EMI) sensors currently feature multi-axis illumination of targets and tri-axial vector sensing, or exploit multi-static array data acquisition [11]. They produce data of high density, quality, and diversity, and have been combined with advanced EMI models to provide superb classification performance [14] relative to the previous generation of single-axis monostatic sensors [15-17]. To take advantage of the rich data sets that these sensors provide, we recently developed and successfully demonstrated a discrimination-oriented data pre-processing scheme based on joint diagonalization (JD) [13]. Let us illustrate the method by describing its TEMTADS implementation. TEMTADS consists of 25 transmit/receive pairs of square coil antennas, each consisting of a 35-centimeter (cm) transmitter loop surrounding a concentric 25-cm receiver coil, arranged in a 5×5 square grid. The sensor activates the transmitter loops in sequence, one at a time, and for each transmitter all receivers receive, measuring the complete transient response over a wide dynamic range of time ranging from approximately 100 microseconds (μs) to 25 milliseconds (ms) and distributed over N_q = 121 time channels. The sensor thus provides 25×25 spatial data points at any given time channel t_q, $q = 1, 2, \ldots, N_q$. If we define $H_{k,m}$ as the z-component of the magnetic field measured by the m-th receiver coil when the k-th transmitter is active, then each row of the measured multi-static response (MSR) data matrix

$$\mathbf{H}(t_q) = \begin{bmatrix} H_{1,1} & H_{1,2} & \cdots & H_{1,M} \\ H_{2,1} & H_{2,2} & \cdots & H_{2,M} \\ \vdots & \vdots & \ddots & \vdots \\ H_{K,1} & H_{K,2} & \cdots & H_{K,M} \end{bmatrix} \tag{3}$$

is a measured data vector for the k-th transmitter, where $k = 1, 2, \ldots, K$. For the TEMTADS system $M = 25$ is the number of receivers and $K = 25$ is the number of transmitters. For each time channel the $M \times K$ MSR matrix can be decomposed into its eigenvectors $\mathbf{U}(t_q)$ and eigenvalues $\mathbf{D}(t_q)$ using the singular value decomposition (SVD) to obtain

$$\mathbf{H}(t_q) = \mathbf{U}(t_q)\mathbf{D}(t_q)\mathbf{U}^T(t_q)\,. \tag{4}$$

However, in order to relate the eigenvalues to the number of potential targets, we need to find a unitary matrix $\mathbf{V}$ of eigenvectors shared by all $\{\mathbf{H}(t_q)\}_{q=1}^{N_q}$ matrices that simultaneously removes all their off-diagonal elements:

$$\mathbf{D}(t_q) = \mathbf{V}^T\mathbf{H}(t_q)\mathbf{V}\,, \qquad q = 1, \ldots, N_q. \tag{5}$$

In general, it is not the case that the matrix $\mathbf{V}$ will cancel all the off-diagonal elements of all the $\mathbf{D}(t_q)$, but a unitary $\mathbf{V}$ can be sought that minimizes the sum of their squares; this is the gist of the JD approach [18]. The diagonal elements of $\mathbf{D}(t_q)$ are the time-dependent eigenvalues of the measured MSR matrix and contain information about the targets that contribute to a given signal. Our studies show that three diagonal elements of the MSR matrix usually suffice to describe one target. We have also found that JD is a robust technique for extracting signals due to targets for data with low signal to noise ratios. See Appendix C for a more detailed exposition of the method.

2.3 EMI Data inversion: A global optimization technique

Determining a buried object's orientation and location is a non-linear problem. Inverse-scattering problems are solved by defining an objective function [5] that measures the mismatch between modeled and measured magnetic-field data and proceeding to find its global minimum. Standard gradient search approaches often suffer from a profusion of local minima that sometimes result in incorrect location and orientation estimates. To avoid this problem we recently adapted and incorporated a different class of global optimization search algorithms, among them differential evolution (DE) [19-20], a heuristic, parallel, direct-search method for minimizing non-linear functions of continuous variables that is straightforward to implement and has good convergence properties. We have combined DE with ONVMS to invert digital geophysical EMI data [5, 14]. All EMI optimizations are split into linear and nonlinear parts, alternating between the two and iterating to minimize the objective function. Once the target locations are found, the amplitudes of the responding ONVMS are determined and used to classify the object relative to the targets of interest.

2.3.1 Discrimination parameters

To classify targets in this demonstration we used ONVMS combined with DE optimization and JD to invert for the locations and electromagnetic signatures of the TOI. The model provides at least three independent principal-axis total ONVMS parameters per target that can be used for discrimination. The total time-dependent ONVMS depends on the size, geometry, and material composition of the object in question: 1) Early time gates bring out the high-frequency response to the shutdown of the exciting field; the induced eddy currents in this range are superficial, and a large total ONVMS amplitude at early times correlates with large objects and large surface area. 2) At late times, when the eddy currents have diffused completely into the object and low-frequency harmonics dominate, the EMI response relates to the metal content (i.e., the volume) of the target. Thus a smaller but compact target has a relatively weak early response that dies down slowly, while a large but thin or hollow object has a strong initial response that decays quickly. Thus the extracted ONVMS parameters can be used to form feature vectors for classification.

2.3.2 Classification approaches

The power-law/exponential-decay parameters extracted from total ONVMS time-decay curves tend to follow definite patterns when TOI of the same kind are interrogated under different conditions. The parameters thus tend to cluster together in ways that provide clues as to the features of the different TOI present in a survey, and by comparing total ONVMS parameters of unknown objects to those of previously characterized targets one can predict the class/cluster to which the unknown targets belong.

There are many clustering techniques available, such as K-means [21], principal component analysis [22], and support vector machines [18, 21, 23-28], which are largely heuristically motivated and do not require an underlying statistical model. A possible alternative is the model-based clustering method, which is based on the assumption that the data are composed of a finite mixture of different distributions of the same type (e.g., multivariate Gaussians) but characterized by different sets of parameters. This procedure has the obvious advantage that it is possible to choose the optimal number of clusters and the distributions that best fit the data using some objective statistical criterion—such as the Akaike Information Criterion (AIC) or the Bayesian Information Criterion (BIC)—while for the other methods those questions are open to discussion.

Clustering methods can also be categorized into unsupervised and supervised. Supervised clustering uses parameters extracted from a set of training/calibration samples, whereas unsupervised clustering applies the same classification criteria to all targets, regardless of size, composition, and decay curves. The former is obviously advantageous in that it utilizes as prior knowledge additional information from the training data. Several supervised clustering techniques like support vector machines [18, 21, 23-28] and template matching have been applied to UXO discrimination. A straightforward approach to implement model-based supervised clustering is to (a) estimate the parameters from the training sample and (b) use the estimated values of the parameters to classify the TOI in the blind test dataset. A drawback of this method is that only the training set is used to estimate the parameters and information from the blind dataset is completely ignored. To avoid this, during this study a semi-supervised

classification algorithm was applied in order to create custom training sets. Decay parameters such as $M_{\alpha\alpha}(t_1)$, and $M_{\alpha\alpha}(t_1)$ / $M_{\alpha\alpha}(t_n)$, where t_n is a given time channel and $M_{\alpha\alpha}$ is the total ONVMS along the α-th axis, were used to cluster the inverted parameters into classes. We assumed that there were K clusters and that each of them was described by a parametric continuous or discrete distribution (e.g., a Gaussian). This let us arrange total ONVMS-extracted time-decay parameters in the $n \times m$ matrix $\mathbf{Y} = [\mathbf{Y}_1, \mathbf{Y}_2, \ldots, \mathbf{Y}_m]$, with n the number of anomalies and m the number of chosen parameters. Taking each $\mathbf{Y}_i$ to follow an m-dimensional mixture of normal distributions allowed us to express the total K-cluster distribution as

$$F(\mathbf{Y}_i) = \sum_{k=1}^{K} w_k f_i(\mathbf{Y}_i \mid \boldsymbol{\mu}_k, \boldsymbol{\sigma}_k), \tag{6}$$

where w_k, is the mixing weight of cluster k, $\Sigma_{k=1}^{K} w_k = 1$, and

$$f_i(\mathbf{Y}_i \mid \boldsymbol{\mu}_k, \boldsymbol{\sigma}_k) = \frac{1}{\sqrt{\boldsymbol{\sigma}_k (2\pi)^m}} \exp\left[-\frac{1}{2} (\mathbf{Y}_i - \boldsymbol{\mu}_k)^T \boldsymbol{\sigma}_k^{-1} (\mathbf{Y}_i - \boldsymbol{\mu}_k) \right] \tag{7}$$

is the probability density of the k-th normal distribution with a mean vector $\boldsymbol{\mu}_k$ (an $m \times 1$ vector) and a variance-covariance matrix $\boldsymbol{\sigma}_k$ (an $m \times m$ matrix). The mixing weight w_k is defined as the proportion of anomalies that belong to the k-th cluster. The parameters $\boldsymbol{\mu}_k$, $\boldsymbol{\sigma}_k$, and w_k are estimated by the maximum likelihood (ML) criterion using the expectation maximization algorithm [29].

2.3.3 Classification using template matching

Template matching is a classification approach that identifies an unknown target by comparing its extracted features—here the total ONVMS—to those of a set stored in a reference library. The comparison can be carried out either 1) by using code that computes least-squares mismatches or 2) by visual inspection. To avoid false negatives and classify targets accurately we used both approaches.

2.4 Details of classification schemes

The discrimination process comprises three sequential tasks: data collection, data inversion, and classification. Each EMI sensor produces unique data sets and therefore requires its own data inversion and classification schemes. This section summarizes the data inversion and classification schemes for the 5 × 5 TEMTADS array and the MM sensor.

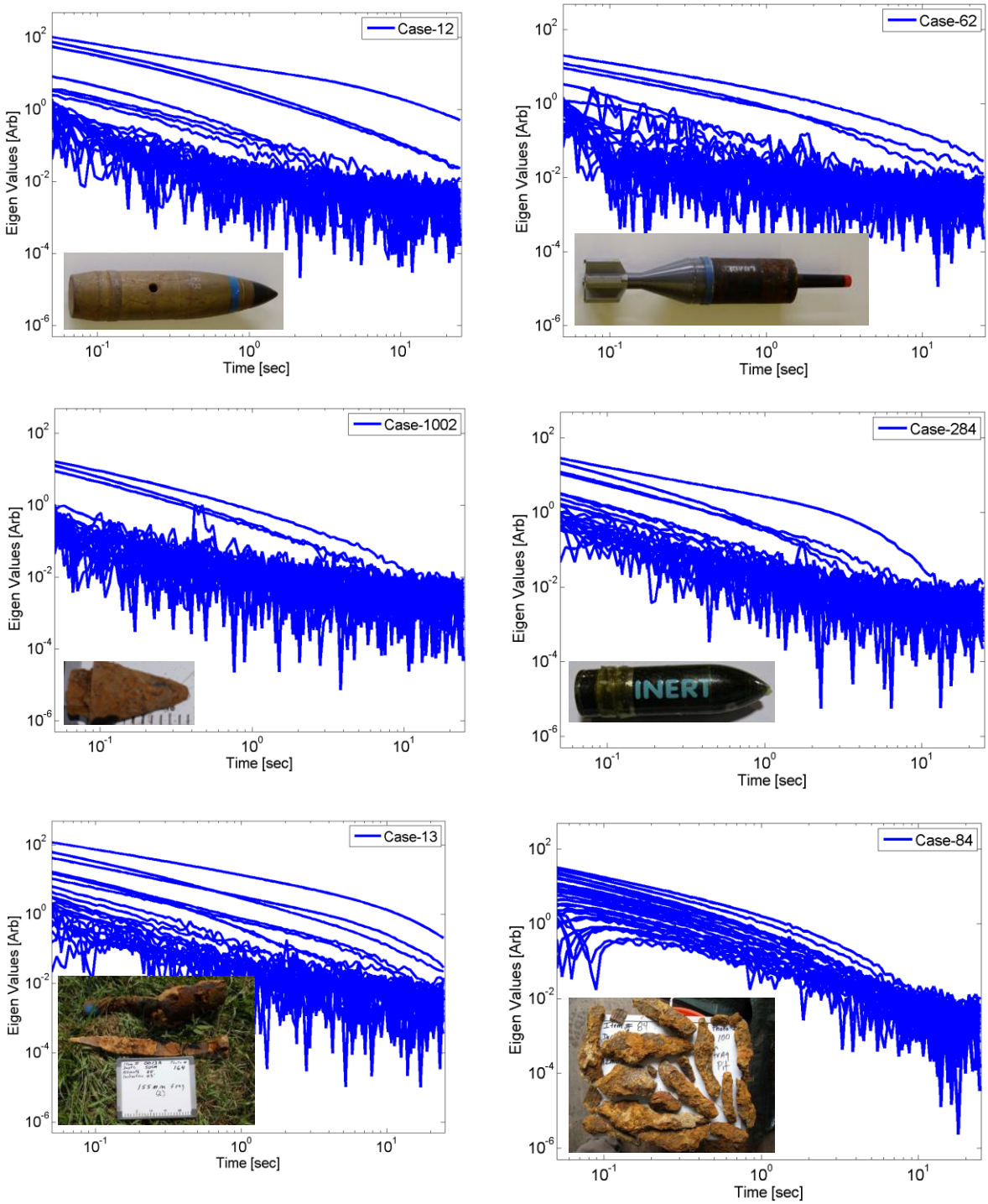

Figure 1. TEMTADS multi-static response matrix eigenvalues versus time for (top row) a 105-mm HE projectile and a 105-mm HEAT round, (center row) an M-48 fuze and a 37-mm munition, and (third row) two clutter scenarios, one with two items (left) and another with several (right).

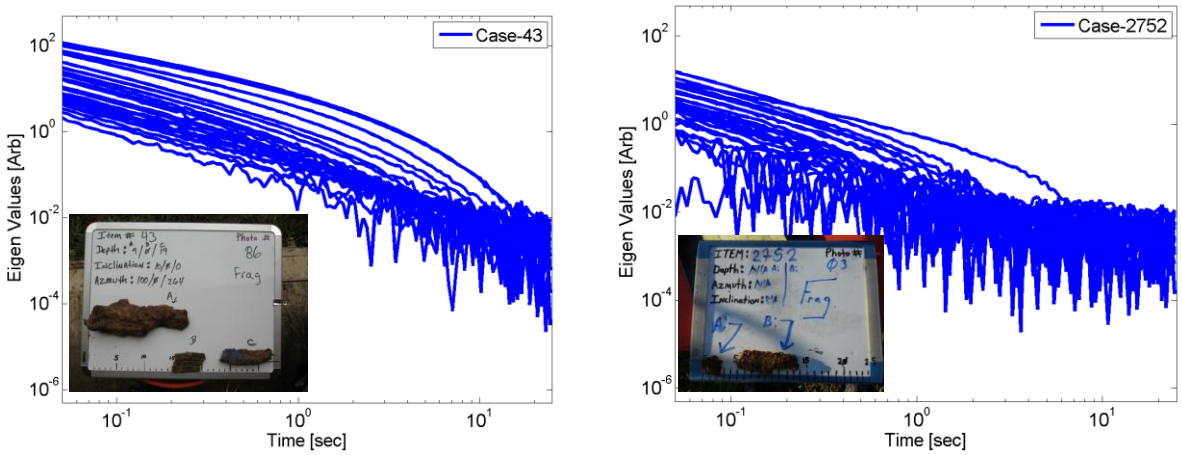

Figure 2. TEMTADS multi-static response matrix eigenvalues versus time for some samples of requested anomalies.

2.4.1 Camp Butner TEMTADS data inversion and classification scheme

The modeling approach used to invert TEMTADS data with the ONVMS-DE algorithm is described in detail in [5]. Here we summarize the main steps employed to invert and classify TEMTADS data for the particular case of Camp Butner.

Step 1. Data pre-processing: All TEMTADS-data were pre-processed using a Matlab code (see Appendix C in [30] that reads comma-delimited CSV files and translates them to ASCII files compatible with the ONVMS-DE code (ONVMS_MM.exe). The user needs only specify the path to the folder with the CSV files; the code then converts them all.

Step 2. Use equation (3) to construct the TEMTADS MSR matrix $\mathbf{H}(t_q)$.

Step 3. Eigenvalue analysis: The JD algorithm constructs a multi-static response matrix using TEMTADS data and computes its eigenvectors and eigenvalues, the latter as a function of time; these are depicted for some of the Camp Butner anomalies in Figure 1 and Figure 2. The eigenvalues of the MSR data matrix are intrinsic properties of the targets, and each target has at least three eigenvalues above the threshold (the noise level is composed of low-magnitude eigenvalues). For example, Figure 1 shows the eigenvalues extracted for a 105-mm HE projectile, a 105-mm HEAT round, an M-48 fuze, a 37-mm projectile, and some clutter items. Each target is seen to have distinguishable eigenvalues, and we used these to make an initial classification. Note that the *magnitudes* of the MSR eigenvalues depend on the depths and orientations of the targets [5], so the user must rely only on their *shapes* when performing JD-based classification. As the number of targets increases (as in Figure 2 and the third row of Figure 1), so does the number of above-noise eigenvalues. We examined the eigenvalues' time-decay curves for each case and used them to estimate the corresponding number of targets.

Step 4. Once we estimated the number of targets and SNR for each anomaly we inverted all cued MM datasets using a multi-target combined ONVMS-DE algorithm. This gave us the extrinsic and intrinsic parameters for all targets, including the total ONVMS as shown in Figure 3 and Figure 4.

Step 5. Create a custom training list using eigenvalue time-decay curves and request the ground truth. For the most part, the JD-based list contained either the anomalies that had too many above-threshold eigenvalues, like the samples depicted in the third row of Figure 1 and in Figure 2, or anomalies which had very small eigenvalues. We requested two batches of training data. The first batch contained 65 anomalies, all of which were clutter; some had six eigenvalues above the noise level, while others had several eigenvalues mixed with the noise. The second batch consisted of 10 anomalies, of which 8 corresponded to UXO.

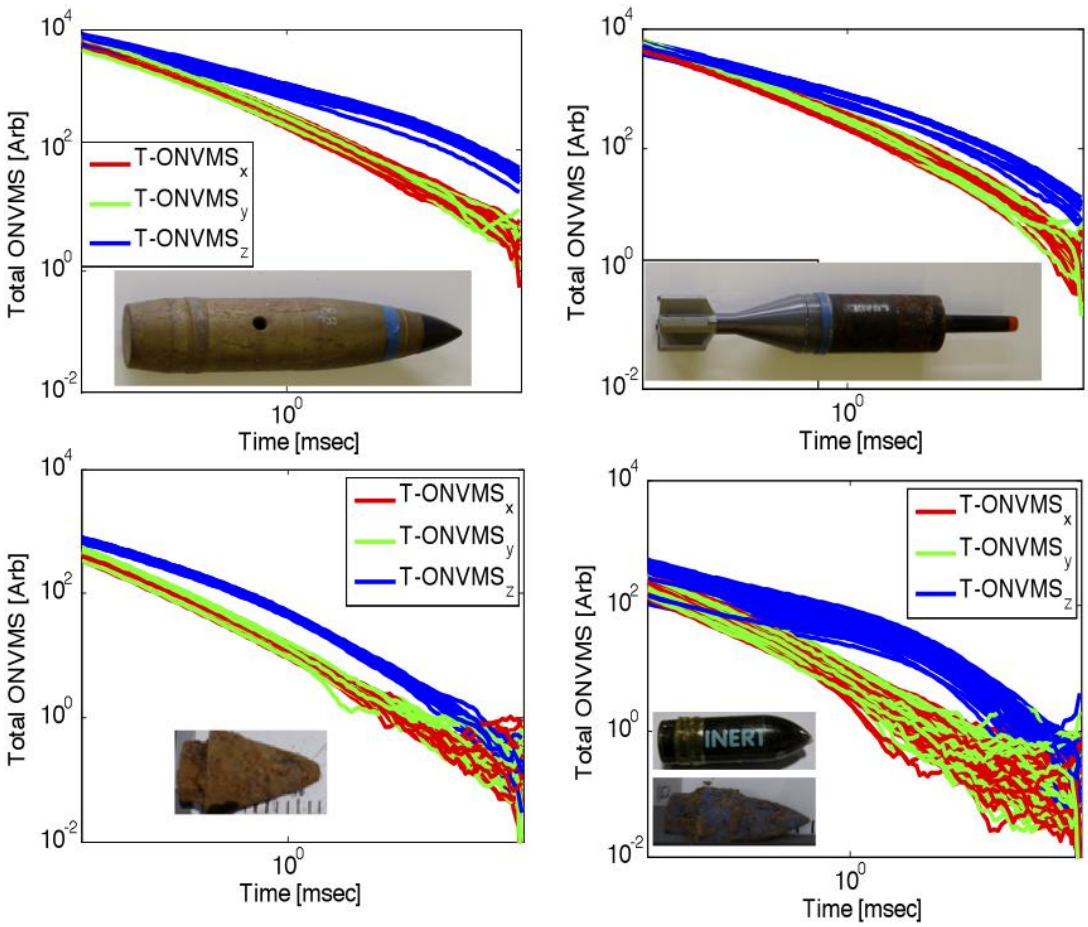

Figure 3: Inverted total ONVMS time-decay profiles for four Camp Butner targets: (top row) 105-mm HE munition and 105-mm HEAT round, and (bottom) M-48 Fuze and 37-mm projectile with copper band.

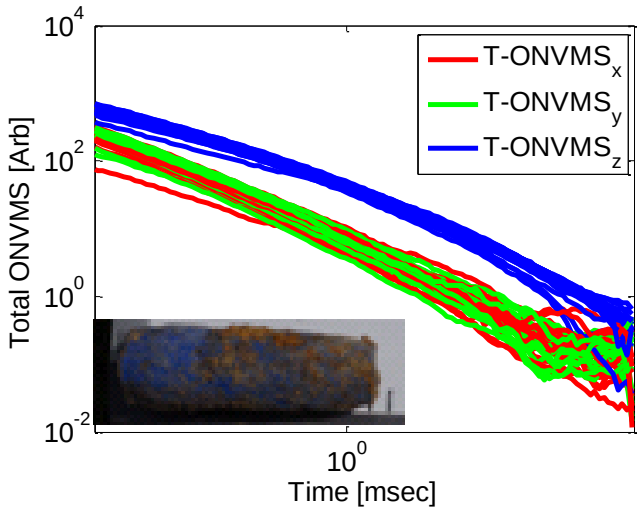

Figure 4: Inverted total ONVMS time-decay profiles for 37-mm projectiles without copper band.

Step 6. Once we had the ground truth for all 75 custom identified anomalies we proceeded to classify all TEMTADS targets using the inverted total ONVMS as discriminating features.

Step 7. Create ranked dig list. Armed with the custom identified training list and the inverted total ONVMS for each case we created a library for M-48 fuzes and 37-mm projectiles without copper band. We did not request training data for either of the 105-mm UXO or for the 37-mm projectile with copper band because we already had TEMTADS test-stand data for these targets. The inverted total ONVMS for the anomalies that were classified as TOI appear in Figure 3 and Figure 4. All the inverted total ONVMS are seen to cluster well, and each target has a total ONVMS with features—such as its amplitude at the first time channel, its decay rate, or the separation between the (blue) primary and (red and green) secondary components at different time channels—that make it amenable to identification. (The most difficult differences to discern were between the M-48 fuzes of Figure 3 and the 37-mm projectiles without copper band of Figure 4). These features allowed us to classify targets as UXO or clutter and also let us sort the UXO by caliber. With this knowledge we created a prioritized dig list that we cross-validated using the time-decay curves of the JD eigenvalues.

Step 8. Submit the dig list to ESTCP. The final prioritized dig list was submitted to the Institute for Defense Analyses (IDA) for independent scoring. The scored results were sent back in the form of a receiver operating characteristic (ROC) curve, which appears in Figure 5. We can see that a) of the 75 targets that were dug for training, 68 targets were not TOI (shift along *x*-axis) and seven were UXO (shift along *y*-axis); b) for 95% TOI classification (the pink dot in Figure 5) only seven extra (false positive) digs are needed; c) to classify all TOI correctly (the light blue dot) only 21 extra (false positive) digs are needed; d) in order to increase the classification confidence, the algorithm requested an additional thirty digs after all TOI had been identified correctly.

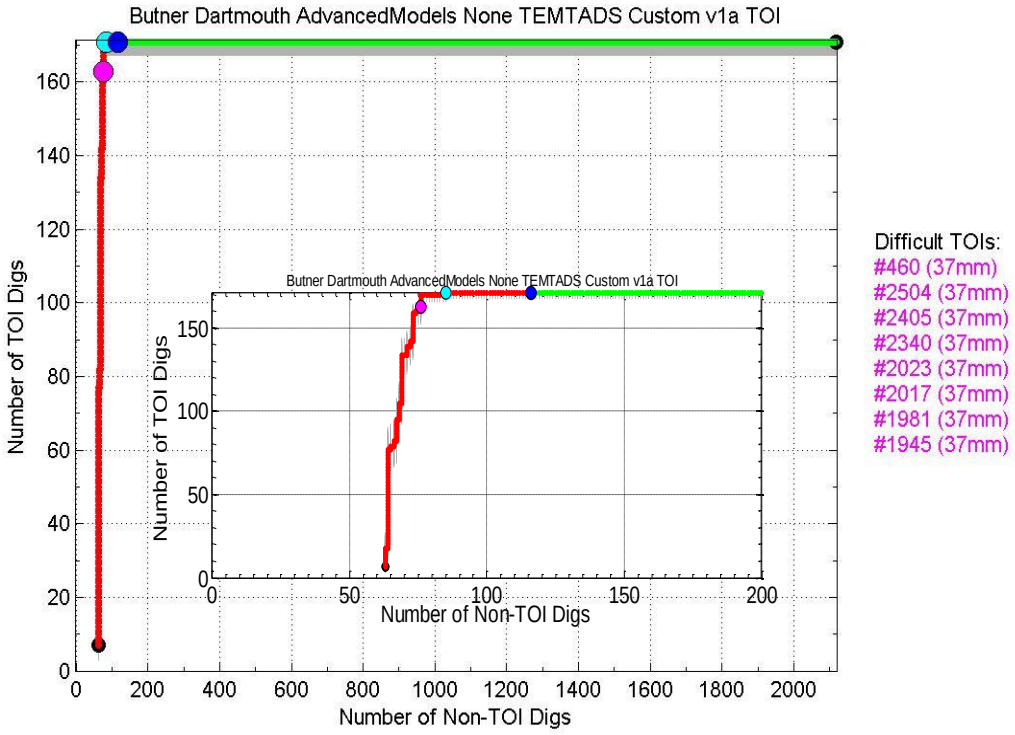

Figure 5. ROC curve for the Camp Butner TEMTADS blind test.

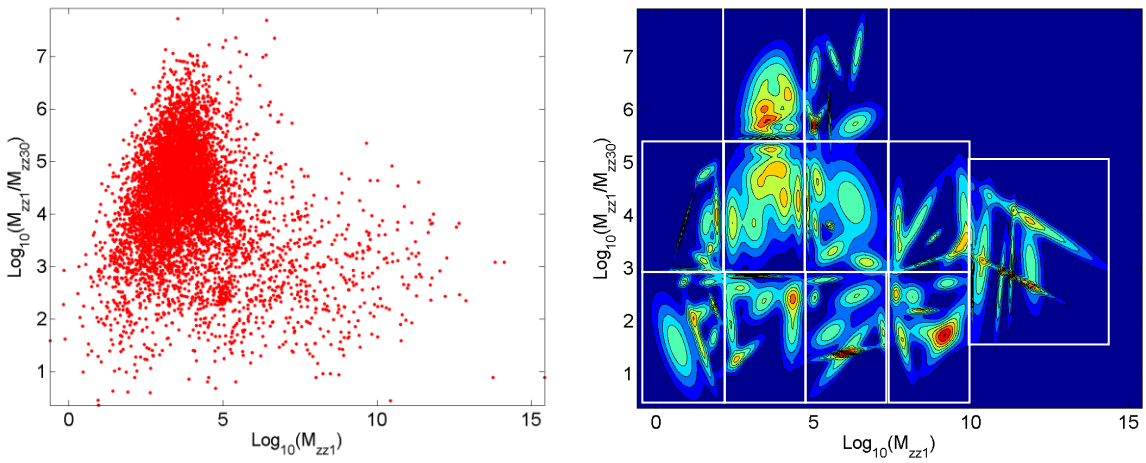

Figure 6: *Left*: Scatter plot for all MM anomalies based on the extracted total ONVMS. *Right*: Probability function for all MM anomalies.

2.4.2 Camp Butner MM data inversion and classification scheme

The Geometrics MetalMapper (MM) is a commercially available advanced EMI sensor. Its geometric configuration is described in [11], and the ONVMS-DE-based modeling approach for inverting the data it provides is described in detail in [5]. The Camp Butner MM cued data sets were collected by teams from Sky Research and Geometrics. A data analysis revealed that the Geometrics MM data had a smaller SNR than the Sky Research data. In addition, it was found that the *y*-receiver of sensor #3 was not working properly when Geometrics took their measurements [11]. To accommodate this prior information it was necessary to exclude this receiver from all Geometrics MM data sets and perform two kinds of classification (statistical and library-matching) to provide cross-checks. Moreover, it was necessary to pay extra attention to the Geometrics MM data when performing library (fingerprint) matching: any anomaly whose primary total ONVMS resembled the total primary ONVMS of any TOI was ranked as a TOI or included in the custom training list. Below we summarize the main steps taken during inversion and classification of Camp Butner MM data.

Step 1. Extract the total ONVMS for each anomaly: We ran the program ONVMS_MM.EXE to extract the parameters for all targets.

Step 2. Create a custom training list: For classification we used the ratio of the inverted total ONVMS at the 30th time channel to that at the first. The values of $\log_{10}[M_{zz}(t_1) / M_{zz}(t_{30})]$ versus $\log_{10}[M_{zz}(t_1)]$ are plotted on Figure 6 (left) for all the data. They clearly exhibit a wide spread of values. To use these features for statistical classification, and for determining clusters and a classification probability function, we first divided the scatter plot of Figure 6 (left) into 11 subsections (shown in the figure). Then to each of these subsections we applied a Gaussian mixture model (implemented as part of Matlab's Statistics Toolbox) assuming that it contained five clusters. (The number of subsections and the number of clusters are not critical at this early stage. We selected the quoted values to ensure that all clusters were found and at the same time to minimize the number of anomalies whose ground truth was

requested.) From the Gaussian mixture model we found the mean and standard deviation for each cluster and built a global classification probability function, depicted in Figure 6 (right).

Step 3. Request the ground truth for selected anomalies: Using the classification probability function we created a first custom training dig list that contained 55 anomalies (i.e., one anomaly for each cluster identified in the preceding step) and requested the ground truth. The success of classification depends on the selection of features, the separation between different classes in feature space, and the ability of the sensor data to constrain the estimated features. We would like to emphasize that in some cases, due to poor signal-to-noise ratio (a particularly common occurrence for Camp Butner Geometrics MM data), the feature vectors from UXO targets were corrupted (see Figure 7) or were similar to those from clutter. In such cases, and given our previous studies (SLO), we recognized that automatic statistical discrimination algorithms had limitations. As a consequence we decided to have the final classification decision be made by expert judgment, overriding automated classification if necessary. This was achieved by inverting all the MM data using the combined ONVMS-DE algorithm as though there were one, two or three targets present and comparing the resulting total ONVMS amplitudes case-by-case. Whenever we spotted significant differences we examined the curves visually, like in the sample case of Figure 7, and, based on this examination, requested the ground truth for an additional 60 Geometrics MM anomalies.

Step 4. Create a ranked dig list: Using the requested ground truth for 121 training anomalies and the the inverted total ONVMS for each case we created libraries for the 105-mm and 37-mm projectiles and the M48 fuzes. The inverted total ONVMS for the anomalies that were correctly correctly classified as TOI appear in Figure 8 and Figure 9. The ground truth from the custom training data set also let us classify all targets as either TOI or not TOI using the probability function of Figure 6 (right). The classification based on the supervised clustering is plotted in Figure 10: the red circles correspond to TOI and the green dots to clutter.

Step 5. Submit the dig list to ESTCP: Using the clustering and library-matching techniques we classified the anomalies as TOI or not TOI. The ranked list was submitted to the IDA for scoring. The results are shown on Figure 11.

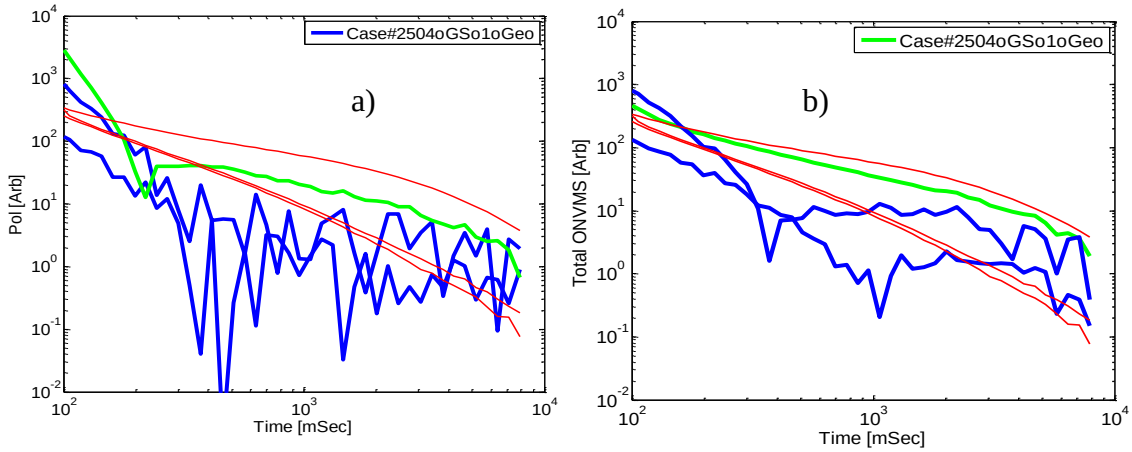

Figure 7: Inverted magnetic dipole polarizability (left) and total ONVMS (right) time-decay profiles for MM anomaly #2504. The thin red lines show a library sample, while the thick blue and green lines show the inversion results.

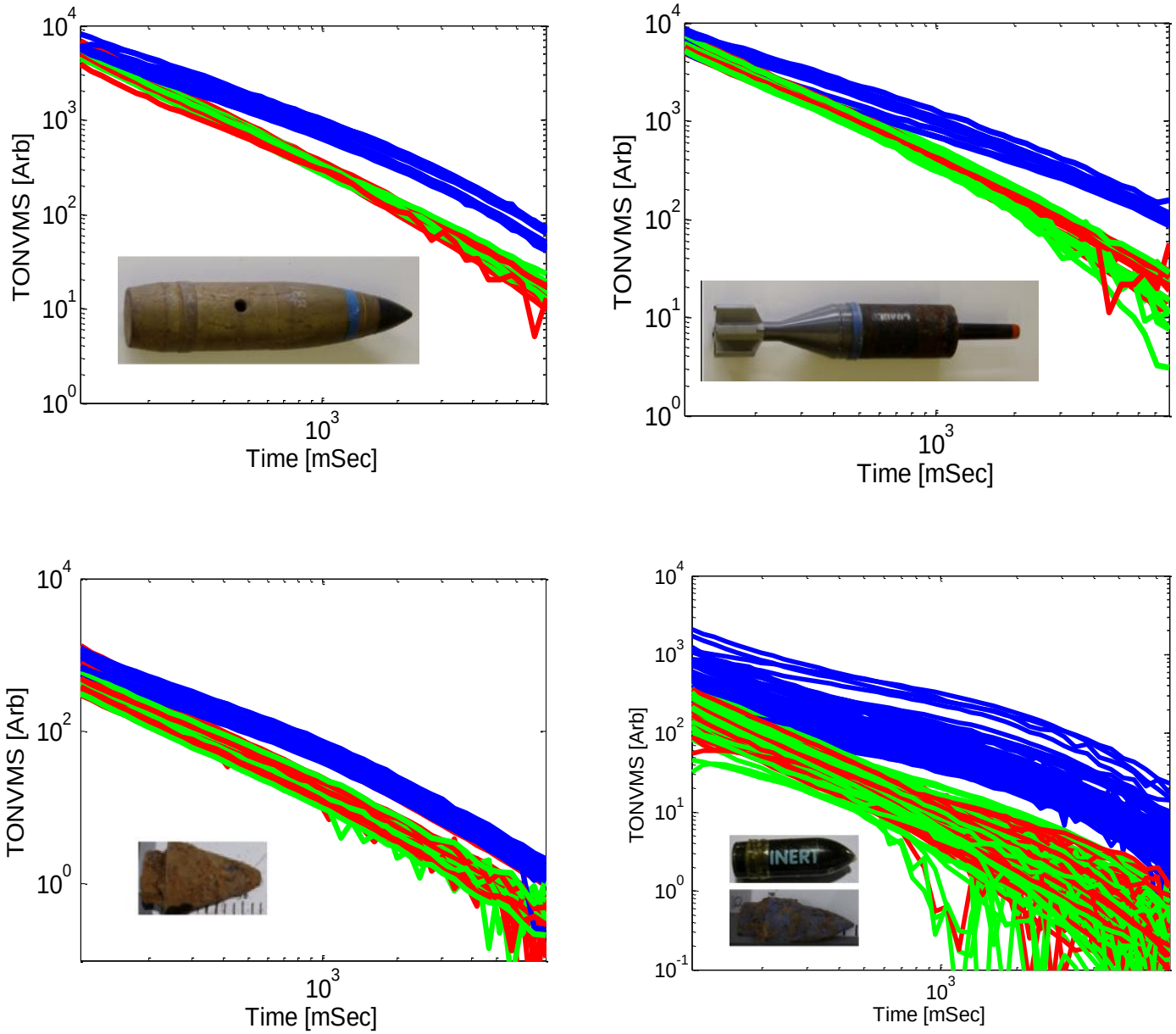

Figure 8. Inverted total ONVMS time-decay profiles from Camp Butner MM data sets: (top row) 105-mm HE shells and 105 mm HEAT rounds, (bottom row) M-48 Fuzes and 37-mm projectiles.

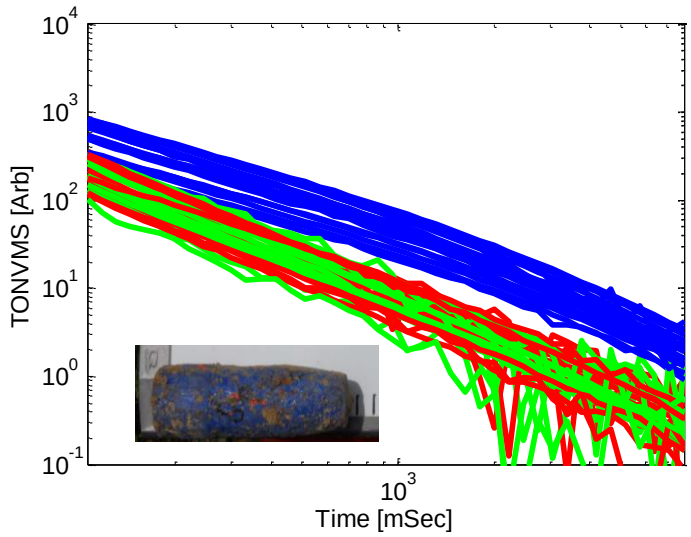

Figure 9. Inverted total ONVMS time-decay profiles from Camp Butner MM data sets for 37-mm projectiles without driving copper bands.

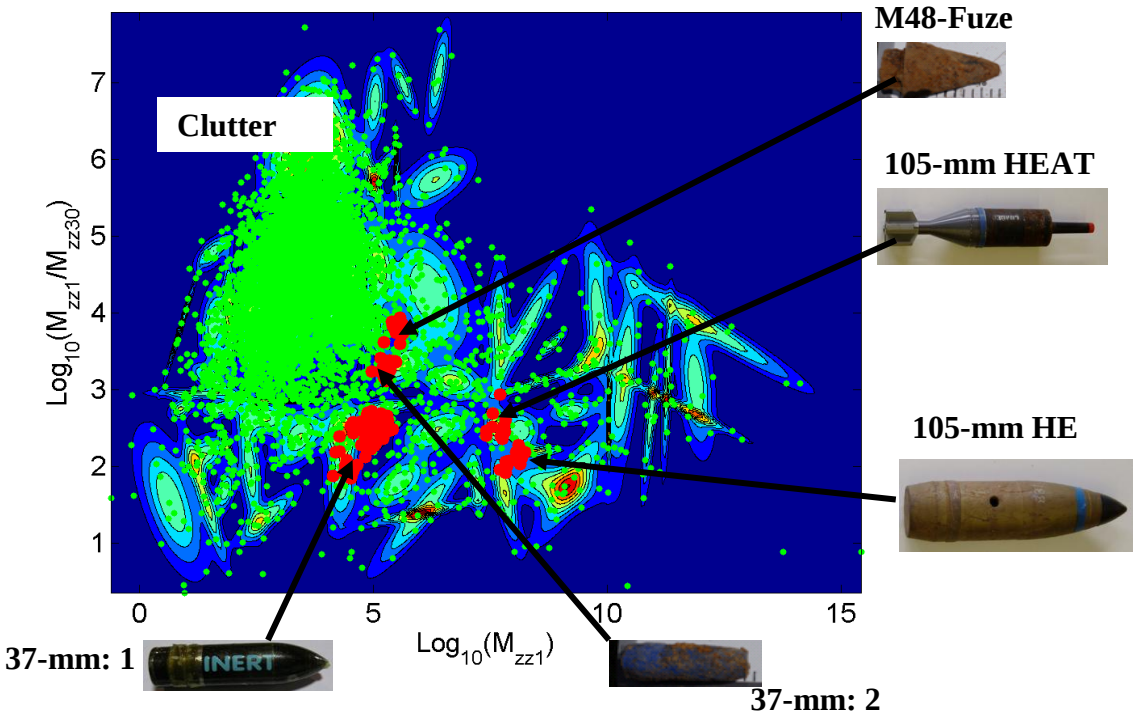

Figure 10: Result of the supervised clustering classification for the Camp Butner MM anomalies using the logarithms of $M_{zz}(t_1)$ / $M_{zz}(t_{30})$ and $M_{zz}(t_1)$. The supervised clustering was trained with calibration data. The green markers correspond to clutter and the red ones to TOI.

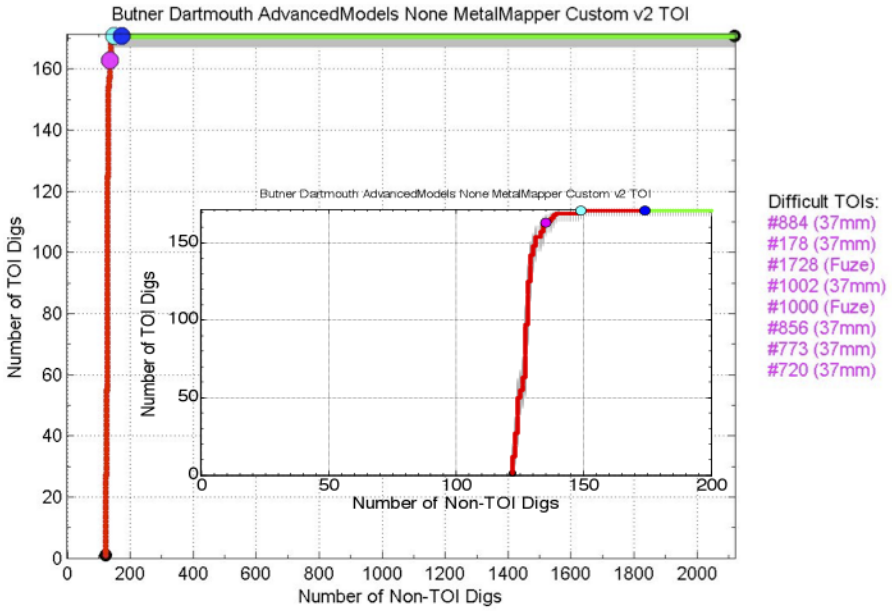

Figure 11: ROC curve for the Camp Butner MetalMapper blind test.

Step 6. The scored results for the 2291 Camp Butner MM anomalies, depicted in Figure 11, show that a) of the 121 targets that were dug for training, 120 targets were not TOI (shift along *x*-axis) and one was (shift along *y*-axis); b) for 95% TOI classification (pink dot in Figure 11) eight extra (false positive) digs are needed; c) to classify all TOI correctly (light blue dot) only 32 additional digs are needed; d) for increased classification confidence the algorithm requested 33 additional digs after all the TOI were identified correctly.

3 PERFORMANCE OBJECTIVES

The performance objectives of this ESTCP live site discrimination study were: to achieve high probability of discrimination of UXO from among a wide spread of clutter; to process all data sets; to minimize the number of data that could not be analyzed or decided upon; to minimize the number of false positives; and to identify all UXO with high confidence. The performance objectives are summarized in Table 1.

Table 1: Performance objectives

Performance Objective	Metric	Data Required	Success Criteria
Maximize correct classification of munitions	Number of targets of interest retained	• Prioritized anomaly lists • Scoring reports from the Institute for Defense Analyses (IDA)	The approach correctly classifies all targets of interest
Maximize correct classification of non-munitions	Number of false alarms eliminated	• Prioritized anomaly lists • Scoring reports from the IDA	Reduction of false alarms by over 75% while retaining all targets of interest
Specification of no-dig threshold	Probability of correct classification and number of false alarms at demonstrator operating point	• Demonstrator-specified threshold • Scoring reports from the IDA	Threshold specified by the demonstrator to achieve the criteria specified above
Minimize the number of anomalies that cannot be analyzed	Number of anomalies that must be classified as “Unable to Analyze”	• Demonstrator target parameters	Reliable target parameters can be estimated for over 90% of anomalies on each sensor’s detection list.
Correct estimation of target parameters	Accuracy of estimated target parameters	• Demonstrator target parameters • Results of intrusive investigation	Total ONVMS ± 10% X, Y < ± 10 cm Z < ± 5 cm size ± 10%

3.1 Objective: maximize correct classification of munitions

An effective technology for discrimination of munitions should maximize the number of targets of interest (TOI) it can classify as such (thus distinguishing them from non-TOI) with high confidence.

3.1.1 Metric

Identify all seeded and native TOI with high confidence using advanced EMI discrimination technologies. (The Program Office did not quantify "high confidence." Our estimates were based on using the extracted total ONVMS as input to statistical classification algorithms and expert judgment. Every anomaly that was close to a TOI cluster in feature space and had $f > 10^{-8}$, where f is the probability density function of equation (7), was considered a possible TOI; the expert then inspected the corresponding TONVMS curve for symmetry (manifested by equal secondary and tertiary TONVMS) and signal-to-noise ratio.)

3.1.2 Data requirements

We analyzed data from two instruments, the 5×5 TEMTADS array and the MetalMapper. For each sensor we identified custom training data sets. We requested the ground truth for the custom training data sets and used it to validate the models for each specific sensor. We generated dig-lists that were scored by the IDA.

3.1.3 Success criteria evaluation and results

The objective was considered to be met if all seeded and native UXO items could be identified below an analyst-specified no-dig threshold.

3.1.4 Results

The objective was successfully met. All TOI, both seeded and native, were identified using our advanced EMI discrimination technology. The ROC curves for the Camp Butner test demonstrate that all TOI were classified correctly, both for TEMTADS (Figure 5) and the MetalMapper (Figure 11).

3.2 Objective: maximize correct classification of non-munitions

The technology aims to minimize the number of false negatives, i.e., maximize the correct classification of non-TOI.

3.2.1 Metric

We compared the number of non-TOI targets that can be left in ground with high confidence using the advanced EMI discrimination technology to the total number of false targets that would be present if the technology were absent.

3.2.2 Data requirements

This objective required prioritized anomaly lists, which our team generated independently for each sensor, and for its evaluation we needed scoring reports from the IDA.

3.2.3 Success criteria evaluation and results

The objective was considered to have been met if the method eliminated at least 75% of targets that did not correspond to TOI in the discrimination step.

3.2.4 Results

This objective was successfully met. The advanced forward EMI models were able to extract robust classification parameters. Using the extracted parameters the classification algorithms were able to eliminate at least 93% of non-TOI targets, as stated by the IDA.

3.3 Objective: specify a no-dig threshold

This project aims to provide a high-confidence classification approach for UXO-site managers. A critical quantity for minimizing the residual risk of UXO and providing regulators with acceptable confidence is a specific no-dig threshold.

3.3.1 Metric

We compared an analyst's no-dig threshold point to the point where 100% of munitions were correctly identified.

3.3.2 Data requirements

To meet this requirement we needed scoring reports from the IDA.

3.3.3 Success criteria evaluation and results

The objective would be met if a sensor-specific dig list placed all the TOI before the no-dig point and if additional digs (false positives) were requested after all TOI were identified correctly.

3.3.4 Results

This objective was successfully met for all data sets (see Figure 5 and

Figure 10). The stop-dig threshold was specified based on the mismatch between the primary total ONVMS for the TOI library items and for the test anomalies. Both the magnitudes and shapes of the time-decay curves were used for the final classification and stop-digging decisions. All uncertain or difficult targets were included in the custom training lists.

3.4 Objective: minimize the number of anomalies that cannot be analyzed

Some anomalies may not be classified, either because of the data are not sufficiently informative—the sensor physically cannot provide the data to support classification for a given target at a given depth—or because the data processing was inadequate. The former is a measure of instrument performance for all anomalies for which all data analysts converge. The latter is a measure of the quality of a data analysis when a target diagnostic differs from those made by other analysts.

3.4.1 Metric

The metric for this objective is the number of anomalies that cannot be analyzed by a particular method, and the intersection of all anomaly lists among all analysts.

3.4.2 Data requirements

Each analyst submitted their anomaly list. IDA scored all lists and returned a list of anomalies that could not be analyzed by any analyst ("cannot analyze" or "failed classification").

3.4.3 Success criteria evaluation and results

The objective was met if at least 95% of a set of selected anomalies could be analyzed.

3.4.4 Results

This objective was successfully met. All four data sets for all anomalies were analyzed. Not a single anomaly was ranked as "cannot analyze."

3.5 Objective: correct estimation of target parameters

The combined ONVMS-DE algorithm provides intrinsic and extrinsic parameters for the different targets. The intrinsic parameters were used for classification, while the extrinsic parameters (i.e., the target locations) were utilized for residual risk assessment.

3.5.1 Metric

The classification results entirely depend on how accurately these parameters are estimated.

3.5.2 Data requirements

To achieve this objective we inverted and tabulated the intrinsic and extrinsic parameters for all targets. To validate extracted extrinsic parameters we needed results of intrusive investigations.

3.5.3 Success criteria evaluation and results

The objective was met if the targets' intrinsic parameters varied within $\pm$10%, the extracted *x-y* location within $\pm$10 cm, and the depth within $\pm$5 cm.

3.5.4 Results

After learning the ground truth for the extrinsic parameters we evaluated the estimates given by our procedure. We look at target depth in more detail, as it is the easiest parameter to compare. Figure 12 and Figure 13 show (for the MetalMapper and TEMTADS, respectively) the distribution of depth errors (defined here by $|Z^{\text{model}} - Z^{\text{data}}|$) The MetalMapper discrepancies have a mean of 4.53 cm and a standard deviation of 4.53 cm; for TEMTADS the mean is 4.37 cm and the standard deviation is 3.76 cm. The agreement between inverted and actual values is good.

The error in horizontal location, defined by $((X^{\text{model}} - X^{\text{data}})^2 + (Y^{\text{model}} - Y^{\text{data}})^2)^{1/2}$, obeys a similar distribution. For the MetalMapper we find a mean of 8.5 cm and a standard deviation of 10.5 cm, while for TEMTADS the mean is 9.3 cm and the standard deviation is 11.4 cm.

We can see that the discrepancies in depth are on average smaller than 5 cm, while the average horizontal error is smaller than 10 cm. Thus the objective was successfully met.

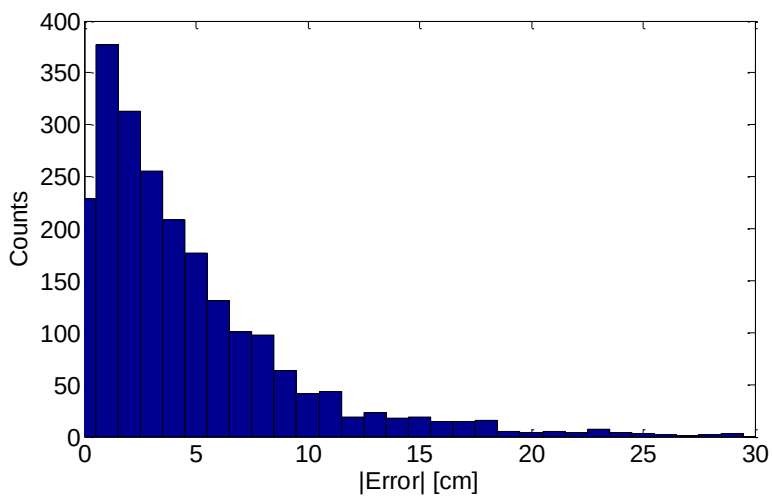

Figure 12. Histogram of depth errors (defined as $|Z^{\text{model}} - Z^{\text{data}}|$) for the set of Camp Butner MetalMapper anomalies. The distribution shown has a mean of 4.53 cm and a standard deviation of 4.53 cm. There is good agreement between the estimates and the ground truth.

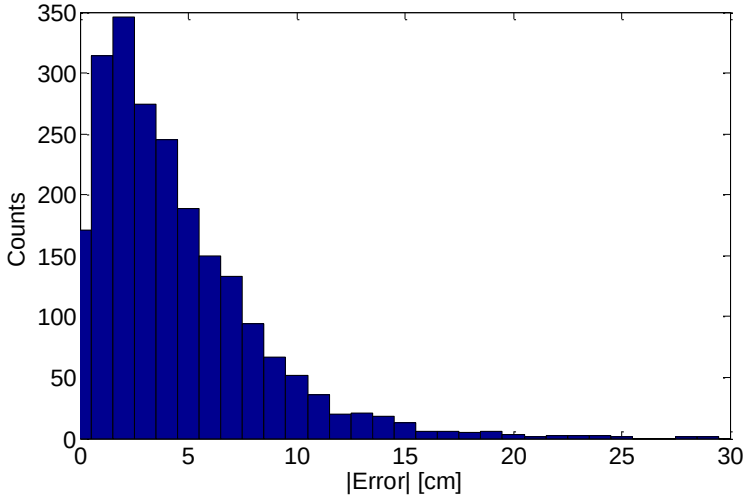

Figure 13. Histogram of depth errors for the Camp Butner TEMTADS anomalies. The mean error here is 4.37 cm and the standard deviation is 3.76 cm. Again we see acceptable agreement with the ground truth.

4 TEST DESIGN

The only required test at the Camp Butner site entailed collecting target characterization training data: Using a calibration pit, the data-collection team made a series of static measurements of example targets at several depths and attitudes in order to cross-check models, confirm Tx and Rx polarity for the sensors, and characterize the so-called "library targets."

4.1 Site preparation

N/A

4.2 Demonstration schedule

	Preparation Calibration	**Blind data set**			**Post-survey analysis**		
Tasks and demonstration stages	**Aug2010**	**Sep '10**	**Oct '10**	**Nov '10**	**Dec '10**	**Jan '11**	**Feb '11**
1. Invert all calibration data	x						
2. Invert 5 × 5 TEMTADS data		x					
3. Invert MM data		x					
4. Build custom training data sets and request ground truth for TEMTADS			x				
5. Build custom training data sets and request ground truth for MM			x				
6. Redefine the MM classifier and request more training data if necessary			x				
7. Redefine the TEMTADS target classifier and request additional training data if necessary			x				
8. Generate MM dig list and submit to IDA				x			
9. Generate TEMTADS dig list and submit to IDA				x			
10. Conduct retrospective analysis if needed					x	x	
REPORTING:							
11. Draft demonstration report						x	
12. Final demonstration report							x

Figure 14. Gantt chart showing a detailed schedule of the activities conducted at Camp Butner.

5 DATA ANALYSIS PLAN

We analyzed all cued data for the MetalMapper and TEMTADS sensors and produced prioritized dig lists for independent scoring.

5.1 Extracting target locations

Target locations were determined relative to the sensor coordinate system using the differential evolution algorithm. Object responses were modeled with ONVMS. This combined ONVMS-DE algorithm was run for single- and multi-target cases and provided target locations.

5.2 Extracting target intrinsic parameters

5.2.1 Single targets

The combined ONVMS-DE algorithm yields the targets' intrinsic total ONVMS, which we used for classification. The total ONVMS contains three moments, $M_{xx}(t)$, $M_{yy}(t)$, and $M_{zz}(t)$, along the primary axes in the target's own reference frame. These moments are similar to simple dipole moment components but carry more information, accounting for the targets' inherent heterogeneities. The ONVMS-DE algorithm outputs the time-decay curves of the target's total ONVMS tensor $M_{ij}(t_k)$. The next step is to determine the time decay of the primary components of the total ONVMS in the target's reference frame. While this can be done by standard diagonalization (i.e., finding $\mathbf{M}(t_k) = \mathbf{V}(t_k)\mathbf{D}(t_k)\mathbf{V}^T(t_k)$, where $\mathbf{V}(t_k)$ contains the eigenvectors of $\mathbf{M}(t_k)$, it is more convenient to perform a joint diagonalization, $\mathbf{M}(t_k) = \mathbf{VD}(t_k)\mathbf{V}^T$, where now the eigenvectors are shared by all time channels; this allows us to extract more reliable total ONVMS values and reduce uncertainty. The resulting temporal decays of the total principal ONVMS for the Camp Butner anomalies are illustrated in Figure 3 and Figure 4 for TEMATDS and in Figure 8 and Figure 9 for the MetalMapper. The results show that the inverted parameters are clustered very well for large targets. As the target size decreases the magnitude of the extracted total ONVMS has a progressively larger spread (especially for MM data), but the *shapes* of the time-decay curves remain the same, indicating that both the shape and the magnitude of the ONVMS should be considered trying to achieve accurate classification.

5.2.2 Multi-target cases

A similar approach is carried out if more than one subsurface target is expected. The DE algorithm now searches for the locations and the total ONVMS of several objects. Such multi-target inversion is crucial in the field for cases in which a signal from a UXO is mixed with EMI signals from nearby clutter. Our two-target inversion code yields three sets of location and total ONVMS estimates: one for Target 1, one for Target 2, and a combined estimate with Targets 1 and 2 represented by a single object. (In the case of 3-target inversion, seven sets of data are expected: only Target 1, only Target 2, only Target 3, Targets 1 and 2 as a single object, Targets 2 and 3 as a single object, Targets 1 and 3 as a single object, and all three targets acting as a single object. In the general case of n targets one expects $n(n-1) + 1$ sets of ONVMS curves).

5.3 Selection of intrinsic parameters for classification

Most UXO are bodies of revolution, and consequently the two secondary polarizability elements are degenerate. However, live-site UXO discrimination studies have repeatedly shown that this symmetry can be compromised due to low SNR, especially for small or deep targets. A good classification of object features can then be obtained by using only the principal component of the total ONVMS, $M_{zz}(t)$. Furthermore, to limit the number of relevant features for use in classification we extract parameters exclusively from the main polarizability $M_{zz}(t)$, both to represent size (via $M_{zz}(t_1)$) and wall thickness (via $M_{zz}(t_1) / M_{zz}(t_n)$). The interested reader is referred to Section 2.4.

5.4 Training

Our classification approach is based on custom training data. At the first stage of the process we used a semi-supervised clustering technique to indentify potential site-specific TOI. Below are the basic steps performed during training data selection; for more details regarding each specific sensor see Section 2.4.

(a) The targets' intrinsic features, $M_{zz}(t_1)$ and $M_{zz}(t_1) / M_{zz}(t_n)$, were selected from the extracted total ONVMS. The time channel n was chosen based on feature separation. EMI data sets were produced for all anomalies using both single- and multi-object inversions.
(b) Initial clustering was performed. The ground truth was requested for all targets whose features were located closest to the corresponding cluster centroid and had TOI-like ONVMS features.
(c) Clusters containing at least one TOI were identified, and a smaller domain was selected within the feature space for further interrogation.
(d) Additional clustering was performed within the selected domain, and those targets with features closest to the corresponding cluster centroids were probed for ground truth. The clusters with at least one identified UXO were marked as *suspicious*. The total ONVMS curves were inspected within the selected domain.
(e) All targets whose features (based on multi-object inversion and library matching) fell inside any of the *suspicious* clusters were used to train the statistical classifier and the library-matching procedure.

5.5 Classification

(f) Probability density functions were extracted for single- and multi-target scenarios.
(g) All of the unknown targets were scored based on the probability density functions.
(h) Dig lists were produced for both single- and multi-object cases and compared to each other to find similarities and differences.
(i) All items were further analyzed using library matching, and all total ONVMS time-decay curves were inspected visually.

(j) A set of anomalies were identified and additional training data sets were requested. The new information was incorporated into the Gaussian mixture model and all items were re-scored.
(k) Based on the previous steps a classification threshold was selected and a final dig list was produced.

5.6 Decision memo

The algorithms used to select training data and to perform inversion and classification for the Camp Butner test are described in Section 2.4. Using the inversion, clustering, classification and data-requesting procedures outlined above we produced a ranked anomaly list formatted as specified by the IDA[31].

6 COST ASSESSMENT

Time and resources were tracked for each task to assess the cost of deploying the technology at future live sites. A summary of the time needed to classify each anomaly successfully appears in Table 2. This assessment does not include actual data-taking, as our team did not perform that work. Neither does it include computer runtime, which usually takes place "in the background" (i.e., concurrently with other tasks, overnight, etc.), nor the one-time cost involved in developing the code. The quoted values are, of course, averages: some anomalies can be identified almost instantaneously, while others require much time and effort. The estimates stem from personal observation—the requirement to systematically keep track of the time was made official after the results had been submitted. Finally, the values given correspond to the times needed by a seasoned expert. Analysts with less experience initially took on average twice as long to identify and classify each anomaly, but quickly became much faster.

Table 2: Cost model for advanced EMI model demonstration at the former Camp Butner

Cost Category	Description	Cost
Pre-processing	Time required to perform eigenvalue extraction, check data quality, and estimate the number of potential anomalies	15 sec/anomaly
Parameter extraction	Time required extract target feature parameters	15 sec/anomaly
Classifier training	Time required to optimize classifier design and train	30 sec/anomaly
Classification and construction of a ranked anomaly list	Time required to classify anomalies in the test set and construct the ranked anomaly list	30 sec/anomaly
	Total	90 sec/anomaly

7 MANAGEMENT AND STAFFING

Figure 15 is the organization chart for the personnel involved in the demonstration. Their responsibilities are as follows:

1. Fridon Shubitidze – Principal Investigator. Developed and implemented most of the preprocessing and inversion routines used. Classified MetalMapper data using a Gaussian mixture model.
2. Irma Shamatava – Sky Research Geophysicist. Participated in the inversion and classification of TEMTADS data.
3. Alex Bijamov – Engineer at Dartmouth College. Classified TEMTADS data via semi-unsupervised parameter clustering.

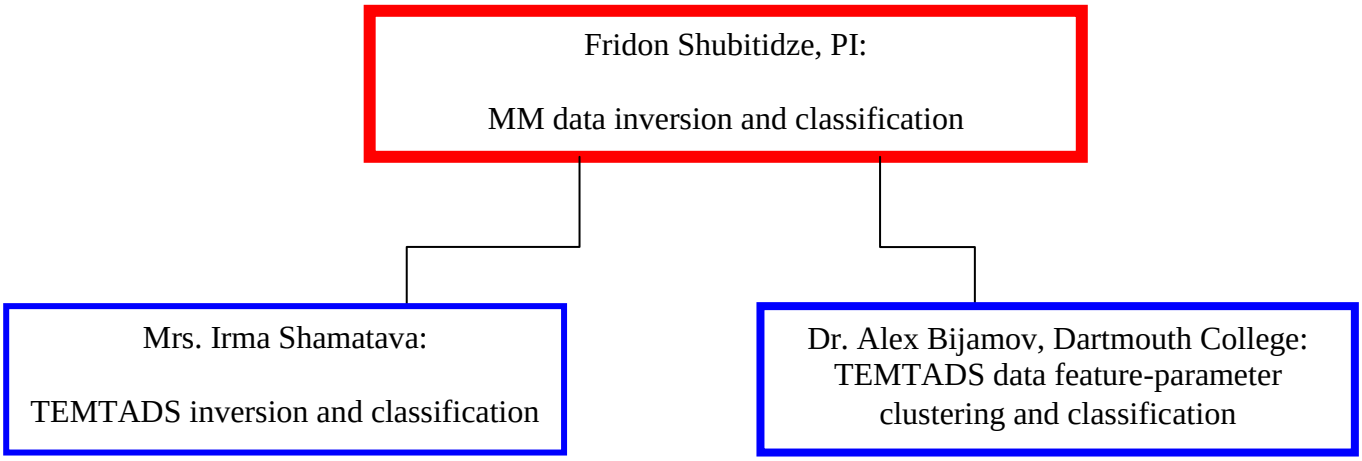

Figure 15: Project management hierarchy.

8 REFERENCES

[1] H. Nelson, *et al.*, "ESTCP Pilot Program, Classification Approaches in Munitions Response," in *Environmental Security Technology Certification Program*, Arlington, VA, 2007.

[2] ESTCP, "2010 ESTCP UXO Classification Study, Former Camp Butner, NC," presented at the Environmental Security Technology Certification Program Demonstration Plan, Arlington, VA, 2010.

[3] ESTCP, "ESTCP Munitions Response, Live Site Demonstrations, former Camp Beale, CA, April 2011, Draft 4," June 2, 2011 2011.

[4] ESTCP, "2009 ESTCP UXO Classification Study, Former Camp San Luis Obispo, CA," presented at the Environmental Security Technology Certification Program Demonstration Plan, Arlington, VA, 2009.

[5] F. Shubitidze, "A complex approach to UXO discrimination: combining advanced EMI forward models and statistical signal processing," Sky Research Inc.2012.

[6] I. Shamatava, *et al.*, "Live-site UXO classification studies using advanced EMI and statistical models," in *SPIE*, 2011.

[7] I. Shamatava, *et al.*, "Applying the physically complete EMI models to the ESTCP Camp Sibert Pilot Study EM-63 data," presented at the Detection and Sensing of Mines, Explosive Objects, and Obscured Targets XIV, Orlando, FL, 2009.

[8] I. Shamatava, *et al.*, "A physically complete model applied to BUD time-domain EMI data," in *SPIE*, 2009, p. 73030N.

[9] I. Shamatava, *et al.*, "Physically complete models applied to BUD time-domain EMI data," presented at the Detection and Sensing of Mines, Explosive Objects, and Obscured Targets XIV, Orlando, FL, 2009.

[10] I. Shamatava, *et al.*, "SLO blind data set inversion and classification using physically complete models," in *SPIE*, 2010, p. 766404.

[11] M. Prouty, "Detection and Classification with the MetalMapper™ at Former Camp San Luis Obispo," presented at the ESTCP Project No. MM-0603, Geometrics, Inc, 2009.

[12] F. Shubitidze, *et al.*, "Application of the normalized surface magnetic charge model to UXO discrimination in cases with overlapping signals," *Journal of Applied Geophysics*, vol. 61, pp. 292-303, 2007.

[13] F. Shubitidze, *et al.*, "Applying a Volume Dipole Distribution Model to Next-Generation Sensor Data for Multi-Object Data Inversion and Discrimination," in *Proceedings of SPIE*, 2010.

[14] F. Shubitidze, "Camp Butner UXO Data Inversion and Classification Using Advanced EMI Models," presented at the SERDP and ESTCP Partners in Environmental Technology Technical Symposium & Workshop, Washington, DC, 2010.

[15] A. Paski, "Former Camp Butner Site Description and EM61 Data Collection and Analysis," presented at the SERDP and ESTCP Partners in Environmental Technology Technical Symposium & Workshop, Washington, DC, 2010.

[16] L. R. Pasion, "UXO Discrimination Using Full Coverage and Cued Interrogation Data Sets at Camp Butner, NC," presented at the SERDP and ESTCP Partners in Environmental Technology Technical Symposium & Workshop, Washington, DC, 2010.

[17] D. Keiswetter, "SAIC Data Analysis of Data Acquired at Camp Butner," presented at the SERDP and ESTCP Partners in Environmental Technology Technical Symposium & Workshop, Washington, DC, 2010.

[18] J. Byrnes, Ed., *Unexploded Ordnance Detection and Mitigation* (NATO Science for Peace and Security Series B: Physics and Biophysics. Dordrecht: Springer Netherlands, 2009, p.^pp. Pages.

[19] R. Storn, "System design by constraint adaptation and differential evolution," *IEEE Transactions on Evolutionary Computation*, vol. 3, pp. 22-34, 1999.

[20] R. Storn and K. Price, "Differential evolution - A simple and efficient heuristic for global optimization over continuous spaces," *Journal of Global Optimization,* vol. 11, pp. 341-359, Dec 1997.

[21] Y. Zhang, *et al.*, "Sensing of unexploded ordnance with magnetometer and induction data: Theory and signal processing," *IEEE Transactions on Geoscience and Remote Sensing,* vol. 41, pp. 1005-1015, 2003.

[22] P. Comon, "Independent Component Analysis, a New Concept," *Signal Processing,* vol. 36, pp. 287-314, Apr 1994.

[23] L. Beran, *et al.*, "A Comparison of Classification Algorithms for UXO Discrimination," presented at the UXO Forum, 2004.

[24] L. Beran and D. W. Oldenburg, "Selecting a discrimination algorithm for unexploded ordnance remediation," *IEEE Transactions on Geoscience and Remote Sensing,* vol. 46, pp. 2547-2557, 2008.

[25] Y. Zhang, *et al.*, "Detection of buried targets via active selection of labeled data: Application to sensing subsurface UXO," *IEEE Transactions on Geoscience and Remote Sensing,* vol. 42, pp. 2535-2543, 2004.

[26] R. E. Grimm, "Triaxial Modeling and Target Classification of Multichannel, Multicomponent EM Data for UXO Discrimination," *Journal of Environmental and Engineering Geophysics,* vol. 8, pp. 239-250, 2003.

[27] J. P. Fernández, *et al.*, "Realistic subsurface anomaly discrimination using electromagnetic induction and an SVM classifier," *EURASIP Journal on Advances in Signal Processing,* vol. 2010, p. 15, 2010.

[28] S. D. Billings, "Discrimination and classification of buried unexploded ordnance using magnetometry," *IEEE Transactions on Geoscience and Remote Sensing,* vol. 42, pp. 1241-1251, 2004.

[29] A. P. Dempster, *et al.*, "Maximum likelihood from incomplete data via the EM algorithm," *Journal of the Royal Statistical Society. Series B (Methodological),* pp. 1-38, 1977.

[30] F. Shubitidze, "Camp Beale Live-Site UXO Data Inversion and Classification Using Advanced EMI Models," Washington, DC2011.

[31] S. Cazares and M. Tuley, "UXO Classification Study: Scoring Memorandum for the former Camp San Luis Obispo, CA," ed: Institute for Defense Analyses, 2009.

[32] G. A. Korn and T. M. Korn, *Mathematical Handbook for Scientists and Engineers*. New York: McGraw-Hill, 1968.

[33] J. E. Gentle, *Matrix algebra : theory, computations, and applications in statistics*. New York, N.Y. ; London: Springer, 2007.

[34] L.-P. Song, *et al.*, "Computing transient electromagnetic responses of a metallic object using a spheroidal excitation approach," *IEEE Geoscience and Remote Sensing Letters*, vol. 5, pp. 359-363, 2008.

[35] J. P. Fernández, *et al.*, "A Man-Portable Vector Sensor for Identification of Unexploded Ordnance," *IEEE Sensors Journal*, vol. 11, pp. 2542-2555, Oct 2011.

[36] A. Belouchrani, *et al.*, "A blind source separation technique using second-order statistics," *IEEE Transactions on Signal Processing*, vol. 45, pp. 434-444, Feb 1997.

[37] S. Harmeling, *et al.*, "Kernel-based nonlinear blind source separation," *Neural Computation*, vol. 15, pp. 1089-1124, May 2003.

[38] B. N. Flury and W. Gautschi, "An Algorithm for Simultaneous Orthogonal Transformation of Several Positive Definite Symmetrical-Matrices to Nearly Diagonal Form," *Siam Journal on Scientific and Statistical Computing*, vol. 7, pp. 169-184, Jan 1986.

[39] J. F. Cardoso and A. Souloumiac, "Jacobi angles for simultaneous diagonalization," *Siam Journal on Matrix Analysis and Applications*, vol. 17, pp. 161-164, Jan 1996.

9 APPENDICES

9.1 Appendix A: Health and Safety Plan (HASP)

As this effort does not involve field data collection, no HASP is required.

9.2 Appendix B: Points of Contact

Points of contact (POCs) involved in the demonstration and their contact information are presented in Table 3.

Table 3: Points of Contact for the advanced EMI models' demonstration

POINT OF CONTACT Name	ORGANIZATION Name Address	Phone Fax E-mail	Role in Project
Dr. Fridon Shubitidze	Sky Research, Inc.	Tel: 603 643 2876 Fax: 603-643-5161 fridon.shubitidze@skyresearch.com	PI
Erik Russell	Sky Research, Inc. 3 Schoolhouse Ln, Etna, NH 03750, USA	Tel: 541-552-5197 Fax: 603-643-5161 Erik.Russell@skyresearch.com	Project Coordinator
Dr. Herb Nelson	ESTCP Program Office, ESTCP Office 901 North Stuart St, Suite 303 Arlington, VA 22203-1821	Tel: 703-696-8726 Herbert.Nelson@osd.mil	ESTCP Munitions Management Program Manager

9.3 Appendix C:

9.3.1 The orthonormalized volume magnetic source model

Most EMI sensors are composed of separate transmitting and receiving coils. When the operator activates the sensor, a current runs through the transmitter, resulting in the establishment of a ("primary" or "principal") magnetic field in the surrounding space (Figure 16). According to the elementary atomic model of matter, all materials are composed of atoms, each with a nucleus and a cloud of orbiting electrons. The electrons cause circulating currents and form microscopic magnetic dipoles. For most materials, in the absence of an external magnetic field the magnetic dipoles of atoms have random orientations, resulting in no magnetic moment. According to Faraday's law, an external time-varying magnetic field induces eddy currents in conducting bodies by an alignment of the magnetic moments of the "spinning" electrons and a magnetic moment due to a change in the orbital motion of electrons. These currents and magnetization in turn generate a ("secondary" or "scattered") magnetic field that also varies with time and induces measurable currents in the receivers. The induced magnetic dipoles/eddy currents are distributed inside the object and produce a magnetic field intensity **H** outside. The magnetic field due to the i-th source can then be expressed at any observation point $\mathbf{r}$ as the matrix-vector productEquation Section (Next)

$$\mathbf{H}_i(\mathbf{r}) = G_i(\mathbf{r})\mathbf{m}_i\,, \tag{A.1}$$

where $\mathbf{m}_i$ is a 1×6 dimensional vector whose components ($M_{xx,i}$, $M_{xy,i}$, $M_{xz,i}$, $M_{yy,i}$, $M_{yz,i}$, $M_{zz,i}$) are the elements of the target's magnetic polarizability tensor $\mathbf{M}$, and $[\Upsilon]$ is the 3×6 matrix

$$G_i(\mathbf{r}) = \frac{1}{4\pi R^5}\begin{bmatrix} \Upsilon_{11} & \Upsilon_{12} & \Upsilon_{13} & \Upsilon_{14} & \Upsilon_{15} & \Upsilon_{16} \\ \Upsilon_{21} & \Upsilon_{22} & \Upsilon_{23} & \Upsilon_{24} & \Upsilon_{25} & \Upsilon_{26} \\ \Upsilon_{31} & \Upsilon_{32} & \Upsilon_{33} & \Upsilon_{34} & \Upsilon_{35} & \Upsilon_{36} \end{bmatrix}, \tag{A.2}$$

whose elements are as follows:

$$\Upsilon_{11} = H_x^{\mathrm{pr}}\left(3R_x^2 - R^2\right) \qquad \Upsilon_{12} = 3R_x\left(R_x H_y^{\mathrm{pr}} + R_y H_x^{\mathrm{pr}}\right) - H_y^{\mathrm{pr}} R^2 \qquad \Upsilon_{13} = 3R_x\left(R_x H_z^{\mathrm{pr}} + R_z H_x^{\mathrm{pr}}\right) - H_z^{\mathrm{pr}} R^2$$

$$\Upsilon_{14} = 3R_x R_y H_y^{\mathrm{pr}} \qquad \Upsilon_{15} = 3R_x\left(R_y H_z^{\mathrm{pr}} + R_z H_y^{\mathrm{pr}}\right) \qquad \Upsilon_{16} = 3R_x R_z H_z^{\mathrm{pr}}$$

$$\Upsilon_{21} = 3R_y R_x H_x^{\mathrm{pr}} \qquad \Upsilon_{22} = 3R_y\left(R_x H_y^{\mathrm{pr}} + R_y H_x^{\mathrm{pr}}\right) - H_x^{\mathrm{pr}} R^2 \qquad \Upsilon_{23} = 3R_y\left(R_x H_z^{\mathrm{pr}} + R_z H_x^{\mathrm{pr}}\right)$$

$$\Upsilon_{24} = H_y^{\mathrm{pr}}\left(3R_y^2 - R^2\right) \qquad \Upsilon_{25} = 3R_y\left(R_y H_z^{\mathrm{pr}} + R_z H_y^{\mathrm{pr}}\right) - H_z^{\mathrm{pr}} R^2 \qquad \Upsilon_{26} = 3R_y R_z H_z^{\mathrm{pr}}$$

$$\Upsilon_{31} = 3R_z R_x H_x^{\mathrm{pr}} \qquad \Upsilon_{32} = 3R_z \left(R_x H_y^{\mathrm{pr}} + R_y H_x^{\mathrm{pr}}\right) \qquad \Upsilon_{33} = 3R_z \left(R_x H_z^{\mathrm{pr}} + R_z H_x^{\mathrm{pr}}\right) - H_x^{\mathrm{pr}} R^2$$

$$\Upsilon_{34} = 3R_z R_y H_y^{\mathrm{pr}} \qquad \Upsilon_{35} = 3R_z \left(R_y H_z^{\mathrm{pr}} + R_z H_y^{\mathrm{pr}}\right) - H_y^{\mathrm{pr}} R^2 \qquad \Upsilon_{36} = H_z^{\mathrm{pr}} \left(3R_z^2 - R^2\right)$$

When there are several such sources, the total field can be expressed as a superposition:

$$\mathbf{H}(\mathbf{r}) = \sum_{i=1}^{M} G_i(\mathbf{r})\mathbf{m}_i = \begin{bmatrix} G_1 & G_2 & \dots \end{bmatrix} \begin{bmatrix} \mathbf{m}_1 \\ \mathbf{m}_2 \\ \vdots \end{bmatrix}. \tag{A.3}$$

Before going further we note that our method takes as input the (in principle unknown) number M of radiating sources. For advanced EMI sensors such as the MetalMapper and 2×2 and 5×5 TEMTADS arrays we have developed a procedure based on joint diagonalization, sketched in Section 9.3.4, that estimates M starting from raw data and with no need for inversion. For other sensors one may proceed by letting M vary as part of an optimization routine.

The superposition (A.3) can be used to carry out one- and multi-object inversions starting from data taken at an ensemble of points. All the measured $\mathbf{H}$-values—which can pertain to multiple transmitters, multiple receivers, changing sensor locations, and different vector components—are strung together in a one-dimensional array, while the corresponding Green functions are stacked as matrix rows. The resulting composite G matrix can then be (pseudo)inverted to find the strengths of the sources. This procedure, which is nothing other than the dipole model if each body is taken to be represented by one source only, works well for one or two sources, but for larger numbers becomes very time-consuming (since the Green matrix becomes very large) and increasingly ill-posed, usually requiring regularization. The ONVMS method is designed to circumvent these difficulties.

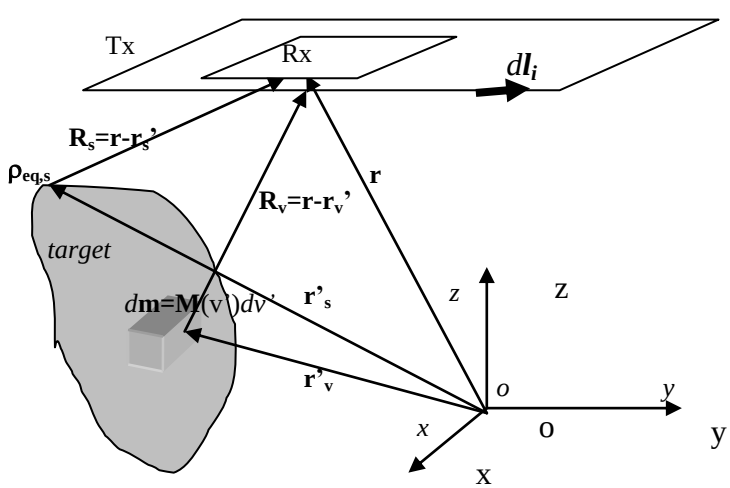

Figure 16: A metallic object under the transmitter. The target's EMI response at the receiver coil can be calculated from the equivalent surface or volume magnetic dipole moment $d\mathbf{m}$.

9.3.2 Orthonormal Green functions

The method starts from the realization that the matrix-vector product (A.1) is valid at any observation point $\mathbf{r}$ and, in particular, at every point $\mathbf{r}_s$ on the plane surface delimited by TEMTADS. If we introduce the inner product

$$\langle A, B \rangle = \int_S A^T B\, ds = \int_{\mathrm{Rx}_0} A^T B\, ds + \int_{\mathrm{Rx}_1} A^T B\, ds + \ldots, \tag{A.4}$$

where the integral is computed over the "sensitive" surfaces of the sensor (which are contiguous in the case of TEMTADS, but not necessarily for other instruments), and if furthermore we can find a basis of Green functions orthogonal under this measure,

$$\mathbf{H}(\mathbf{r}_s) = \sum_{j=1}^{M} \Psi_j(\mathbf{r}_s)\mathbf{b}_j \quad \text{such that} \quad \langle \Psi_j, \Psi_k \rangle = F_j \delta_{jk}, \tag{A.5}$$

where δ_{jk} is a Kronecker delta, then it is possible to find the source amplitudes $\mathbf{b}_j$ without costly and ill-conditioned inversions simply by exploiting the sifting property of the orthogonal basis:

$$\langle \Psi_k, \mathbf{H} \rangle = \sum_{j=1}^{M} \langle \Psi_k, \Psi_j \rangle \mathbf{b}_j = \sum_{j=1}^{M} F_k \delta_{kj} \mathbf{b}_j = F_k \mathbf{b}_k \tag{A.6}$$

and thus

$$\mathbf{b}_k = F_k^{-1} \langle \Psi_k, \mathbf{H} \rangle, \tag{A.7}$$

which clearly does not involve solving a linear system of equations; it is necessary to invert only the 6×6 matrix F_k. Moreover, this definition of the coefficients $\mathbf{b}_j$ guarantees that they are "optimal" in the sense that the expansion (A.5) yields the least mean-square error $\left\langle \mathbf{H} - \Sigma_{j=1}^{M} \Psi_j \mathbf{b}_j, \mathbf{H} - \Sigma_{j=1}^{M} \Psi_j \mathbf{b}_j \right\rangle$ [32].

To construct the set of orthonormal Green functions we resort to a generalization of the Gram-Schmidt procedure [33]. Assuming that the Green matrices are linearly independent—i.e., that we cannot have a collection of distinctly located dipole sources combining to produce no measurable field unless their amplitudes all vanish—we define

$$
\begin{aligned}
\Psi_1 &= G_1, \\
\Psi_2 &= G_2 - \Psi_1 A_{21}, \\
&\vdots \\
\Psi_m &= G_m - \sum_{k=1}^{m-1} \Psi_k A_{mk}, \\
&\vdots \\
\Psi_M &= G_M - \sum_{k=1}^{M-1} \Psi_k A_{Mk},
\end{aligned}
\tag{A.8}
$$

where the 6×6 matrices A_{jk} obey $A_{jk} = 0$ for $j \le k$. Enforcing the orthogonality relation (A.5) is equivalent to setting $\langle \Psi_n, G_m \rangle = F_n A_{mn}$ for $n < m$, and using this relation twice in definition (A.8) we find that

$$
A_{mn} = F_n^{-1} \left(C_{nm} - \sum_{k=1}^{n-1} A_{nk}^T F_k A_{mk} \right), \tag{A.9}
$$

where the overlap integral $C_{mn} = \langle G_m, G_n \rangle$.

At the end of the process it is necessary to recover an expansion expressed, like (A.1), in terms of the actual Green functions, in part because the functions Ψ_j are orthogonal (and defined) only at points on the receivers, and in part because of the non-uniqueness of the coefficients $\mathbf{b}_j$ due to the arbitrary order in which the G_j enter the recursion (A.8). To that end, we express

$$
\Psi_m = \sum_{k=1}^{m} G_k B_{mk} , \tag{A.10}
$$

and to find the coefficients B_{mk} we compare expansion (A.10) term by term to the definition (A.8) and use the rule that $A_{jk} = 0$ for $j \le k$ to find

$$
\begin{aligned}
B_{mm} &= I, \text{ the identity}, \\
B_{m(m-1)} &= -A_{m(m-1)}, \\
B_{mq} &= -\sum_{l=q}^{m-1} B_{lq} A_{ml} \quad \text{for } 1 \le q \le m-2,
\end{aligned}
\tag{A.11}
$$

in terms of which we recover the physical polarizability elements:

$$
\mathbf{H} = \sum_{k=1}^{M} \Psi_k \mathbf{b}_k = \sum_{k=1}^{M} \left(\sum_{l=1}^{k} G_l B_{kl} \right) \mathbf{b}_k = \sum_{l=1}^{M} G_l \left(\sum_{k=l}^{M} B_{kl} \mathbf{b}_k \right) = \sum_{l=1}^{M} G_l \mathbf{m}_l . \tag{A.12}
$$

9.3.3 ONVMS procedure

With all the pieces in place, we can sketch an algorithm to invert EMI data using the ONVMS model:

1) Given a number of sources and their tentative locations, find the Green tensors G_i using equation (A.2) and compute the overlap integrals G_{mn} using the inner product (A.4).

2) Determine the first normalization factor, $F_1 = \langle G_1, G_1 \rangle$, and use it to find all the Gram-Schmidt coefficients A_{mn} with $n = 1$: $A_{m1} = F_1^{-1} C_{1m}$.

3) Set $m = 2$; compute, in sequence,

   a) The coefficients A_{mn} with $n = 2, \ldots, m-1$ using equation (A.9);

   b) The function Ψ_m using the expansion (A.8);

   c) The normalization factor $F_m = \langle \Psi_m, \Psi_m \rangle$;

   increase m by 1 and iterate until all sources have been included.

4) Once all the A_{mn}, F_m, and Ψ_m are known, find B_{mq} using (A.11).

5) Use the orthonormality of the new Green functions to determine the source amplitudes using $\mathbf{b}_q = F_q^{-1} \langle \Psi_q, \mathbf{H}^{\text{data}} \rangle$, as in (A.7). Take the measured field to be piecewise constant—i.e., constant throughout each receiver—when evaluating the integrals.

6) Use the computed $\mathbf{b}_q$, B_{mq}, and G_m, along with the expansion (A.12), to generate the secondary field prescribed by the given number of sources at the given locations.

7) Compare the model prediction with the measured data, vary the source locations, and iterate until the least-squares discrepancy between prediction and measurement attains a suitable minimum.

The procedure as written applies to only one time gate, but the extension to fully time-dependent functions is straightforward: we need only substitute the vectors $\mathbf{b}_q$ and $\mathbf{H}^{\text{data}}$ for two-dimensional arrays where the columns denote time. The relations between the two, namely (A.7) and (A.12), acquire multiple right-hand-sides, and the optimization mentioned on Step 7 of the algorithm is constrained further. As a final remark we note that rigorously speaking the

coefficients $\mathbf{b}_q$ (and, for that matter, the amplitudes $\mathbf{m}_k$) are *not* the polarizabilities themselves but relate more closely to their time derivatives [34-35].

The great advantage of the ONVMS technique is that it takes into account mutual couplings between different parts of targets and avoids matrix singularity problems in cases with multiple objects. Once the polarizability tensor elements and the locations of the elemental responding dipoles are determined one can group them according to their volume distribution. For each group a total polarizability tensor can be computed and diagonalized using joint diagonalization, the topic of Section 9.3.4. The resulting time-dependent diagonal elements have been shown to be intrinsic to the objects and can be used, on their own or combined with other quantities, in discrimination processing.

9.3.4 Joint diagonalization for multi-target data pre-processing

In real-life situations the targets of interest are usually surrounded by natural and artificial debris with metallic content, including, for instance, the remains of ordnance that did explode. Thus it is usually not clear how many objects are producing a given detected signal; all sensing methods, including EMI, are fraught with detection rates that overwhelm cleanup efforts and hike their cost. Here we introduce a data pre-processing technique based on joint diagonalization (JD) that estimates the number of targets present in the field of view of the sensor as it takes a data shot, and, in a good number of cases, even provides the capability to perform real-time characterization and classification of the targets without the need for a forward model.

Joint diagonalization has become an important tool for signal processing and inverse problems, used as part of independent component analysis [22], blind source separation or BSS [36], common principal component analysis, and, more recently, kernel-based nonlinear BSS [37]. We further extend the applicability of the method by using it to detect and locate buried targets without the need for inversion. As we say above, a variation of the method can be used to extricate time-dependent electromagnetic signatures from attitude information. Here we will outline the detailed procedure as applied to the TEMTADS sensor array, a time-domain device with 25 transmitter/receiver pairs that provides 625 measurements over N_g = 123 time gates at each sensor location. Equation Section (Next)

9.3.5 The multi-static response matrix

JD estimates the eigenvalues and eigenvectors of a square time- or frequency-dependent multi-static response (MSR) matrix synthesized directly from measured values. To construct the MSR matrices one just has to stack the 625 readings at each time gate in a 25 × 25 array so that each column stands for one of N_t transmitters and each row represents one of N_r receivers:

$$\mathbf{S}(t_k) = \begin{bmatrix} H_{11} & H_{12} & \cdots & H_{1N_t} \\ H_{21} & H_{22} & \cdots & H_{2N_t} \\ \vdots & \vdots & \ddots & \vdots \\ H_{N_r 1} & H_{N_r 2} & \cdots & H_{N_r N_t} \end{bmatrix}, \quad k = 1, \ldots, N_g, \tag{B.1}$$

where the element H_{ij} is the field measured by the i-th receiver when the j-th transmitter is fired. The second step of the procedure is to diagonalize the 123 matrices at one stroke so they all share a single set of orthonormal eigenvectors. In other words, given the MSR matrix $\mathbf{S}(t_k)$ at the k-th time gate, we look for a unitary matrix $\mathbf{V}$ such that the products

$$\mathbf{D}_k = \mathbf{V}^T \mathbf{S}(t_k)\mathbf{V} \tag{B.2}$$

are "as diagonal as possible" (i.e., their off-diagonal elements vanish within a preset tolerance). By diagonalizing all the matrices simultaneously we separate the time-dependent intrinsic features of the responding sources (and hence the interred objects), which get encapsulated in the eigenvalues, from the other factors—notably the location and orientation of the target with respect to the sensor—that influence the signal but do not change as the data are being taken; these get bundled into the eigenvectors. (The fact that the locations and orientations can be dissociated in this way from the electromagnetic signatures is an upside of the low frequencies of the quasistatic EMI range, because the relevant Green functions are time-independent.) Thus the measured data can be resolved as a superposition of "elemental" sub-signals, each corresponding to an elementary dipolar source, whose combination corresponds to the buried objects. Each source—and the corresponding field singularity—can moreover be localized numerically: the TEMTADS geometry is such that the diagonal of the unprocessed MSR matrix mimics a set of monostatic measurements, akin to those taken with a handheld sensor, which peak sharply when there is a target directly underneath. The maxima in the diagonal thus point to the transmitter/receiver pairs closest to any responding sources. These location estimates can be grouped and correlated to the eigenvalue distributions to estimate target locations.

9.3.6 Interpretation and diagonalization of the MSR matrix

We now proceed to express our above considerations quantitatively. Initially we consider the transmitter assembly, which in TEMTADS consists of a set of coplanar square loops forming a regular grid. The Biot-Savart law gives the primary magnetic induction established at the location $\mathbf{r}_i$ of the l-th source when the j-th transmitter antenna (whose area is σ_{Tx_j}) is excited immediately before shutoff by a current I_j:

$$\mathbf{B}_{jl}^{\mathrm{pr}} = \frac{\mu_0 I_j}{4\pi}\sigma_{\mathrm{Tx}_j}\frac{1}{\sigma_{\mathrm{Tx}_j}}\oint_{\mathrm{Tx}_j}\frac{d\mathbf{l}' \times (\mathbf{r}_l - \mathbf{r}')}{|\mathbf{r}_l - \mathbf{r}'|^3} = \mathbf{g}_{jl}^{\mathrm{pr}}\sigma_{\mathrm{Tx}_j} I_j\,. \tag{B.3}$$

This primary field induces in the l-th source a dipole moment given by

$$\mathbf{m}_{jl} = \mathbf{U}_l \mathbf{\Lambda}_l \mathbf{U}_l^T \mathbf{B}_{jl}^{\mathrm{pr}}\,, \tag{B.4}$$

where the Euler rotation matrix $\mathbf{U}$ relates the instrument's coordinate axes to the principal axes of the source, and the diagonal polarizability matrix $\mathbf{\Lambda}_i$, the only quantity intrinsic to the source, measures the strength with which the primary field induces a moment along each of those axes.

According to Faraday's law, the signal measured by a receiver coil is the electromotive force given by the negative of the time derivative of the secondary magnetic flux through the coil. Since the field at point $\mathbf{r}$ of a dipole of moment $\mathbf{m}$ placed at $\mathbf{r}_0$ is given by

$$\mathbf{B} = \frac{\mu_0}{4\pi} \nabla \times \left(\mathbf{m} \times \frac{\mathbf{r} - \mathbf{r}_0}{|\mathbf{r} - \mathbf{r}_0|^3} \right), \quad \text{and thus} \quad \int \mathbf{B} \cdot d\mathbf{s} = -\mathbf{m} \cdot \frac{\mu_0}{4\pi} \oint d\mathbf{l} \times \frac{\mathbf{r} - \mathbf{r}_0}{|\mathbf{r} - \mathbf{r}_0|^3}$$

by straightforward application of Stokes's theorem, one obtains that the signal sampled at time t_k by the i-th receiver (of area σ_{Rx_i}) when the l-th source is excited by the j-th transmitter is

$$\begin{aligned} H_{ij}^{l}(t_k)\sigma_{\mathrm{Rx}_i}\sigma_{\mathrm{Tx}_j} I_j &= \frac{\mu_0}{4\pi}\sigma_{\mathrm{Rx}_i} \frac{1}{\sigma_{\mathrm{Rx}_i}} \oint_{\mathrm{Rx}_i} \frac{d\mathbf{l}_i' \times (\mathbf{r}' - \mathbf{r}_l)}{|\mathbf{r}' - \mathbf{r}_l|^3} \cdot \dot{\mathbf{m}}_{jl}(t_k) = \mathbf{g}_{li}^{\mathrm{sc}} \sigma_{\mathrm{Rx}_i} \cdot \dot{\mathbf{m}}_{jl}(t_k) \\ &= \mathbf{g}_{li}^{\mathrm{sc}} \sigma_{\mathrm{Rx}_i} \cdot [\mathbf{U}\dot{\mathbf{\Lambda}}_l(t_k)\mathbf{U}^T] \cdot \mathbf{g}_{jl}^{\mathrm{pr}} \sigma_{\mathrm{Tx}_j} I_j, \end{aligned} \tag{B.5}$$

where a dot over a variable indicates its time derivative. In equations (B.3) and (B.5) the line element $d\mathbf{l}'$ lies on the x-y plane, and as a consequence the Green functions are similar in structure to those of the simple model presented in Section 2.2. Note that we have included the exciting current I_j and the transmitter and receiver areas in the definition of the signal; we have explicit knowledge of these quantities and can factor them out. If only the l-th source is illuminated, we construct the MSR matrix for the complete transmitter/receiver array by tiling $N_r \times N_t$ instances of the expression (B.5):

$$\mathbf{S} = \mathbf{G}^{\mathrm{sc}} \mathbf{U}_l \mathbf{\Lambda}_l \mathbf{U}_l^T (\mathbf{G}^{\mathrm{pr}})^T, \tag{B.6}$$

where the primary (or transmitter) dyad $\mathbf{G}^{\mathrm{pr}}$ is of size $N_t \times 3$, the secondary (or receiver) dyad $\mathbf{G}^{\mathrm{sc}}$ is of size $N_r \times 3$, and the response matrix $\mathbf{U}\mathbf{\Lambda}_l\mathbf{U}^T$ is 3×3. When there is more than one source present, the MSR matrix of equation (B.6) is readily generalized:

$$\begin{aligned} \mathbf{S} &= \begin{bmatrix} \mathbf{G}_1^{\mathrm{sc}} & \mathbf{G}_2^{\mathrm{sc}} & \ldots \end{bmatrix} \begin{bmatrix} \mathbf{U}_1\dot{\mathbf{\Lambda}}_1\mathbf{U}_1^T & 0 & \cdots \\ 0 & \mathbf{U}_2\dot{\mathbf{\Lambda}}_2\mathbf{U}_2^T & \cdots \\ \vdots & \vdots & \ddots \end{bmatrix} \begin{bmatrix} (\mathbf{G}_1^{\mathrm{pr}})^T \\ (\mathbf{G}_2^{\mathrm{pr}})^T \\ \vdots \end{bmatrix} \\ &= \begin{bmatrix} \mathbf{G}_1^{\mathrm{sc}}\mathbf{U}_1 & \mathbf{G}_2^{\mathrm{sc}}\mathbf{U}_2 & \ldots \end{bmatrix} \begin{bmatrix} \dot{\mathbf{\Lambda}}_1 & 0 & \cdots \\ 0 & \dot{\mathbf{\Lambda}}_2 & \cdots \\ \vdots & \vdots & \ddots \end{bmatrix}, \end{aligned} \tag{B.7}$$

where we see that the features intrinsic to the targets can be separated formally from the particulars of the measurement—that is, from the geometry and dimensions of the sensor and the sensor-target attitude. The array $\mathbf{S}$ has size $N_r \times N_t$ and is square if $N_r = N_t$, as is the case with TEMTADS. This allows us to diagonalize the matrix but does not suffice to guarantee that the extracted information is useful—i.e., that the eigenvalues and eigenvectors are real, and that the latter are orthonormal. For that to hold we must have a real, symmetric matrix, which requires $\mathbf{G}_l^{\mathrm{sc}} = \mathbf{G}_l^{\mathrm{pr}} \equiv \mathbf{G}_l$. This cannot be rigorously true, because the receivers cannot coincide exactly with the transmitters, but holds approximately for TEMTADS if we factor the exciting current and the coil areas out of $\mathbf{S}$, as we did in equation (B.5). The diagonalization we perform is thus a particular case of a singular value decomposition (SVD), and in what follows we use "diagonalization" as shorthand for "SVD of a symmetric matrix."

The decomposition (B.7) exhibits the actual polarizability elements but is not directly available to us because the Green tensors are not orthogonal. To see what we do get when we diagonalize **S** we can perform the SVD on **G**:

$$\mathbf{S} = \mathbf{G}\mathbf{U}\boldsymbol{\Lambda}\mathbf{U}^T\mathbf{G}^T = \mathbf{W}\left[\boldsymbol{\Sigma}\mathbf{V}^T\mathbf{U}\boldsymbol{\Lambda}\mathbf{U}^T\mathbf{V}\boldsymbol{\Sigma}\right]\mathbf{W}^T = \mathbf{W}\mathbf{Z}\boldsymbol{\Delta}\mathbf{Z}^T\mathbf{W}^T = \mathbf{Y}\boldsymbol{\Delta}\mathbf{Y}^T \tag{B.8}$$

In the intermediate step we have used the fact that the matrix within the brackets is real and symmetric and thus has a purely real eigendecomposition. Result (B.8) shows that the eigenvalue matrix $\boldsymbol{\Delta}$, though time-dependent, is not solely composed of source responses, but also contains location and orientation information extracted from the Green tensors. The eigenvectors, likewise, include information from both the polarizabilities and the measurement particulars.

We also see in the decomposition (B.8) that **S** contains an unknown "hidden dimension"—3*N*, where *N* is the number of sources—in the size of the block-diagonal response matrix. Numerical diagonalization (or, in general, the SVD) of **S** will impose this middle dimension to be $N_r = N_t$. Ideally, the method should be able to resolve up to $\lfloor N_r / 3 \rfloor$ responding sources, or eight for TEMTADS, but the actual number is lower. For one, the procedure will resolve targets only when they are spatially separated: two distinct dipoles sharing one location decrease the rank of the **G** matrices, and hence of **S**, by 3. In any case, diagonalization of **S** can again let us estimate the number of targets illuminated by the sensor; since the only time-dependent quantities are the intrinsic polarizabilities of the sources, we expect the additional information provided by the time decay of the eigenvalues to be useful for classification.

The development outlined above corresponds to each time gate taken separately. To make sense of the time-dependent information we have to find a way to "follow" each of the eigenvalues as the signal decays. (A similar process must be carried out when using the dipole model for inversion.) One could in principle diagonalize the MSR matrix at each time channel, and the eigenvectors, which depend only on geometry and pose, should stay constant; however, it is not possible to know a priori the order in which the eigenvalues will be given by the diagonalization; this fact—not to mention noise and experimental uncertainty—makes it inevitable to have to disentangle the tensor elements by hand, which is easily done wrong. Instead, we explicitly look for an orthogonal matrix of eigenvectors that diagonalizes all the MSR matrices simultaneously. The procedure we employ is a generalization of the method for single matrices, and is well-known; it is sketched in next Section.

9.3.7 Algorithm for joint diagonalization

The joint diagonalization algorithm we use [36, 38-39] is a generalization of Jacobi's procedure to find the eigenvalues of a single matrix. Formally we set out to solve the optimization problem

$$\begin{aligned} \min_V \quad & \frac{1}{2}\sum_{q=1}^{N_g}\sum_{i\neq j}([VA(t_q)V^T]_{ij})^2 \\ \text{s.t.} \quad & V^TV = I, \end{aligned} \tag{B.9}$$

which we accomplish by making repeated Givens-Jacobi similarity transformations designed to gradually accumulate the "content" of the matrices on their diagonals until a certain tolerance

level is reached. The transformations are of the form $A(t_q) \rightarrow A'(t_q) = V_{rs} A(t_q) V_{rs}^T$, with the matrix V_{rs} being the identity but with the four elements V_{rr}, V_{rs}, V_{sr}, and V_{ss} replaced by the two-dimensional rotation array

$$\begin{bmatrix} \cos\phi_{rs} & \sin\phi_{rs} \\ -\sin\phi_{rs} & \cos\phi_{rs} \end{bmatrix}, \quad \text{with} \quad \tan 2\phi_{rs} = \frac{f_{rs}}{n_{rs} + \sqrt{f_{rs}^2 + n_{rs}^2}}, \tag{B.10}$$

where

$$n_{rs} = \sum_q \left\{ a_{rr}(t_q) - a_{ss}(t_q)]^2 - [a_{rs}(t_q) + a_{sr}(t_q)]^2 \right\}, \tag{B.11}$$

$$f_{rs} = 2\sum_q [a_{rr}(t_q) - a_{ss}(t_q)][a_{rs}(t_q) + a_{sr}(t_q)]. \tag{B.12}$$

The indices are swept systematically, and the procedure is repeated until convergence is reached. The computational burden is equivalent to that of diagonalizing the matrices one by one. The resulting eigenvalues and eigenvectors are all real because all the MSR matrices are symmetric.